J. Fluid Mech. (1981), *vol.* 113, *pp.* 347–386
Printed in Great Britain

A preliminary investigation of the interaction of internal gravity waves with a steady shearing motion

By C. GARY KOOP

Fluid Mechanics Department, TRW Defense and Space Systems Group,
Redondo Beach, California 90278

(Received 5 September 1980 and in revised form 23 March 1981)

Preliminary experimental results are presented which describe the interaction of an internal-wave field with a steady shearing motion. The results are primarily qualitative and presented in the form of photographs of shadowgraph images. Several internal-wave sources are used, and both critical- and non-critical-layer flows are examined. The results of these observations are interpreted in terms of several existing theories. For critical-layer flows the primary result is that virtually none of the internal-wave momentum flux penetrates the critical-level region, and under certain conditions a critical-layer instability develops resulting in the generation of turbulence. Such wave-induced turbulence is also observed for certain non-critical-layer flows and is believed to be the result of a convective instability.

1. Introduction

Within about the past decade, as a result of numerous and extensive field-measurement programmes, a wealth of information has been obtained regarding the nature of the subsurface oceanic environment. One of the more difficult tasks in these investigations has been the characterization of the ambient levels of shear which exist in the upper regions of the ocean arising from such processes as large-scale geostrophic motions (eddies), intrusions and low-frequency inertial waves. The measurements of Sanford (1975), made during the Mode 1 experiment, reveal that shear levels $\partial u/\partial z = O(10^{-3}\text{–}10^{-2}\,\mathrm{s}^{-1})$ are not an uncommon feature of the thermocline region, with the bulk of this shear being attributable to internal waves on inertial scales. In terms of Richardson numbers, these data show, at least at the Mode 1 measurement site, that roughly 90 % of the water column was characterized by gradient Richardson-number levels lying in the range $\frac{1}{4} < Ri < 4$. It is clear that such levels of shear are apt to have important dynamical effects upon the higher-frequency portion of the internal-wave spectrum.

The intent of the present paper is to examine experimentally, albeit in a qualitative fashion (*via* photographs of shadowgraph images), what effects the presence of a velocity field may have on an internal-wave field. In a subsequent paper we will deal with the character of this flow field in a more quantitative manner. The experimental apparatus used in this investigation is a modified and scaled-up version of a device first discussed by Odell & Kovasznay (1971). The unique feature of this facility is its ability to generate a relatively steady shearing motion in a fluid which is continuously stratified for time scales of at least 10 min and perhaps even longer. Much of the previous experimental work in this area has dealt with layered fluids but it will

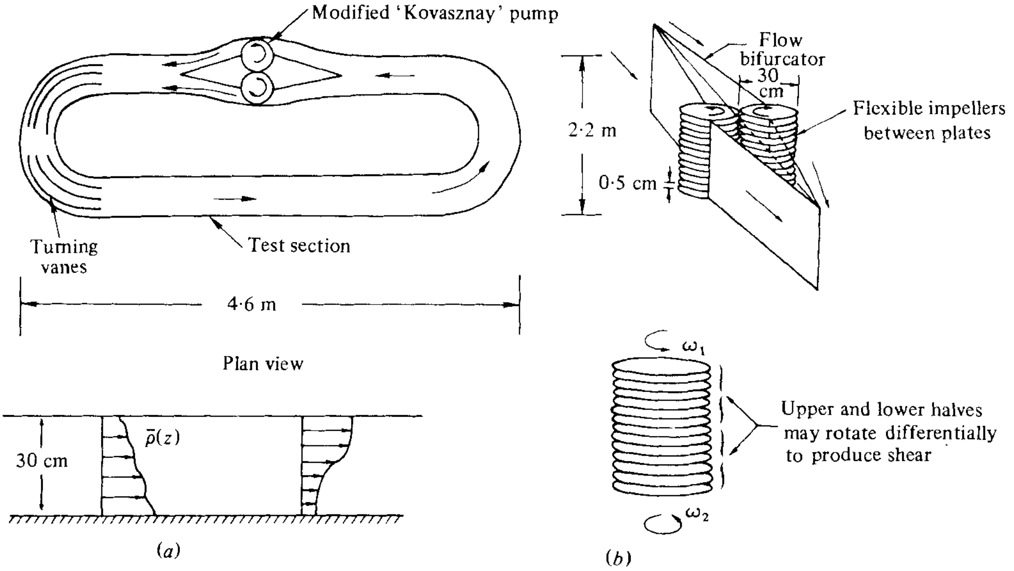

FIGURE 1. (*a*) Schematic of the stratified shear-flow facility. (*b*) Detail of the pumping mechanism.

be shown subsequently that many of the interesting features of the internal-wave/mean-flow interaction may be exhibited only when the ambient medium has continuous variations.

The first series of experiments deal with the wave field generated by an oscillating cylinder in order to study the interaction of the mean flow with a simple constant-frequency disturbance. The remainder of the paper deals with internal-wave/shear interactions for both critical- and non-critical-layer flows. For this portion of the study two internal-wave sources were used, the first being a sinusoidally corrugated boundary of large horizontal extent which was towed through the test section of the facility. The wave patterns generated by this monochromatic source are amenable to analytic calculation, and the resulting flow field is interpreted in terms of existing theory. In addition, a towed circular cylinder was also used as an internal-wave source in order to study the character of an internal-wave/shear interaction subject to an internal-wave forcing which is broad-banded and spatially compact.

2. Experimental apparatus

The experiments to be described were performed in a newly developed stratified-shear flow facility which is shown schematically in figure 1 and photographically in figure 2. Basically, the facility consists of an annular tank having a test section of 30 x 45 cm cross-section and 3 m in length which is continuously stratified using saline solutions. The fluid moves around the channel under the action of a pumping mechanism, depicted in figure 1 (*b*), which was modelled after a device first discussed by Odell & Kovasznay (1971). Essentially, the pump consists of two vertical stacks of circular plates which counter-rotate and impart momentum to the incoming fluid while preserving the structure of the ambient stratification down to length scales comparable to the plate spacing (approx. 0·5 cm). In the original model of Odell &

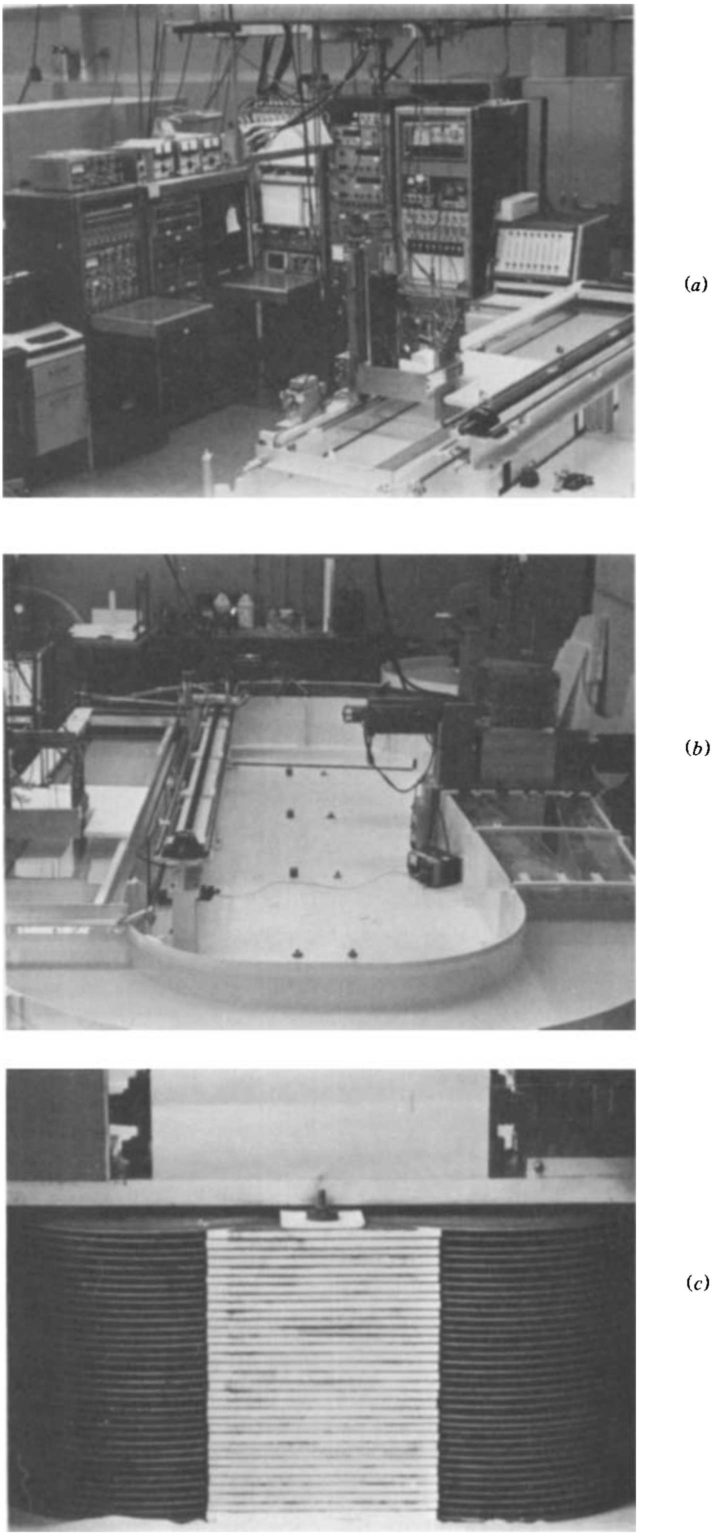

FIGURE 2. Photographs of the stratified shear-flow facility: (*a*) electronics, (*b*) shear-flow tank, (*c*) detail of pump.

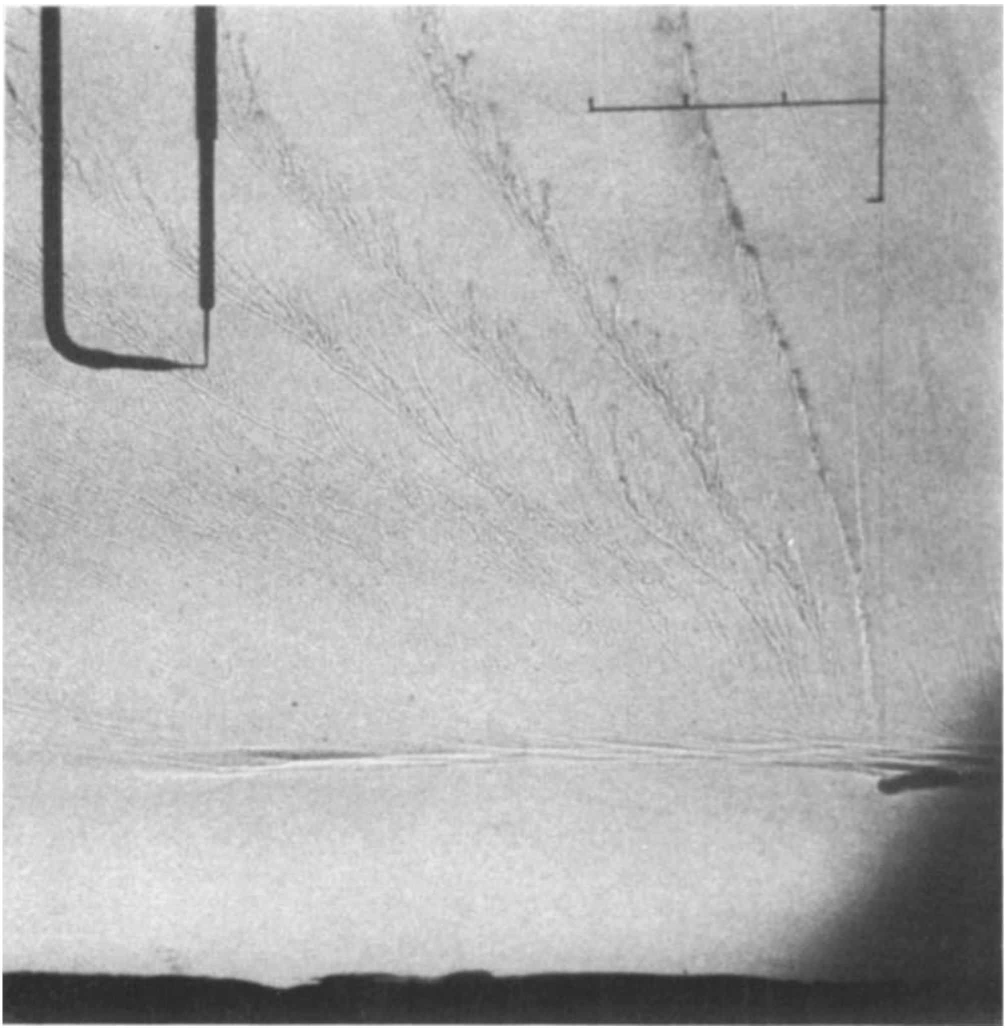

FIGURE 3. Example of pulsed hydrogen-bubble wire trace used to measure the mean velocity profile. The total vertical scale in the figure is 4 cm. For the most recent bubble trace the tick marks on the horizontal scale correspond to 1 cm s^{-1}. This figure also shows the probe configuration used in figure 25.

Kovasznay viscous spin-up by the circular plates was used to accelerate the incoming fluid. In the present apparatus (which is considerably larger) this proved to be a somewhat inefficient means of pumping the fluid. To alleviate this difficulty, flexible impellers were introduced in between the plates so that momentum is transferred to the incoming fluid under the action of a positive-displacement piston-type motion. With this modification, flow velocities in the range of 0–10 cm s^{-1} are readily generated. For practical operation, however, maximum fluid velocities were typically less than 5 cm s^{-1}. Above this limit, turbulence produced by the pump and boundary layers on the bottom and sidewalls adversely affected the flow in the test section. For fluid velocities less than 5 cm s^{-1}, however, the flow in the test section was quite laminar, and turbulent motions generated by the pumping action, turning vanes or sidewall boundary layers were rarely observed. We note here that these conclusions are

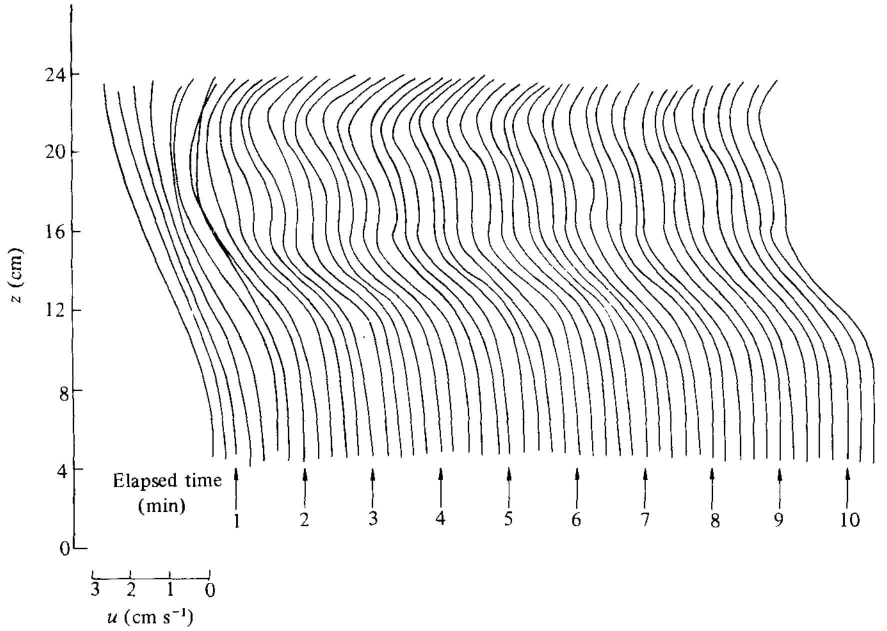

FIGURE 4. Evolution of velocity profile measured using pulsed hydrogen-bubble wire. Profiles offset by 0·35 cm s^{-1}.

based upon observations of the flow field made with rather strong stratification ($N \simeq 2{\cdot}5\ \mathrm{s}^{-1}$). However, we have also operated the channel using significantly weaker stratification (fluid velocities of 2·5 cm s^{-1} and Brunt–Väisälä frequency $N = 1{\cdot}2\ \mathrm{s}^{-1}$) with a minimal amount of turbulence being observed.

A second modification made to the original idea of Kovasznay was the introduction of a double-gearing system, coupled with two independent drive motors, which allows the upper halves of the two stacks to rotate differentially with respect to the lower halves.† In this manner, a greater amount of momentum may be imparted to the fluid in (say) the upper half of the tank, so that a shearing motion in the fluid is generated. For most of the experiments to be described, we attempted to keep the fluid in the lower portion of the tank stationary and propel the upper-half fluid around the tank. As an interesting sidelight, we found that to maintain the lower half of the fluid stationary in the test section it was necessary to rotate the lower plates at a very slow rate in order to overcome pressure gradients presumably generated by a slight degree of baroclinicity.

Velocity-profile measurements were made using a pulsed hydrogen-bubble wire generator, an example of which is shown in figure 3. This method was chosen primarily owing to its simplicity together with its ability to provide fairly detailed quantitative information about the vertical structure of the profile. One slight disadvantage of this technique is that the bubbles are buoyant when they are swept off the wire. However, for steady flows and slow bubble-rise velocities the locus of the bubble path closely follows the mean velocity profile, the net effect being a bubble depopulation in the lower regions of the tank (which is almost quiescent, anyway). We remark here that

---

† Structural considerations require that both halves be rotated in the same direction, thus precluding counter-rotation.

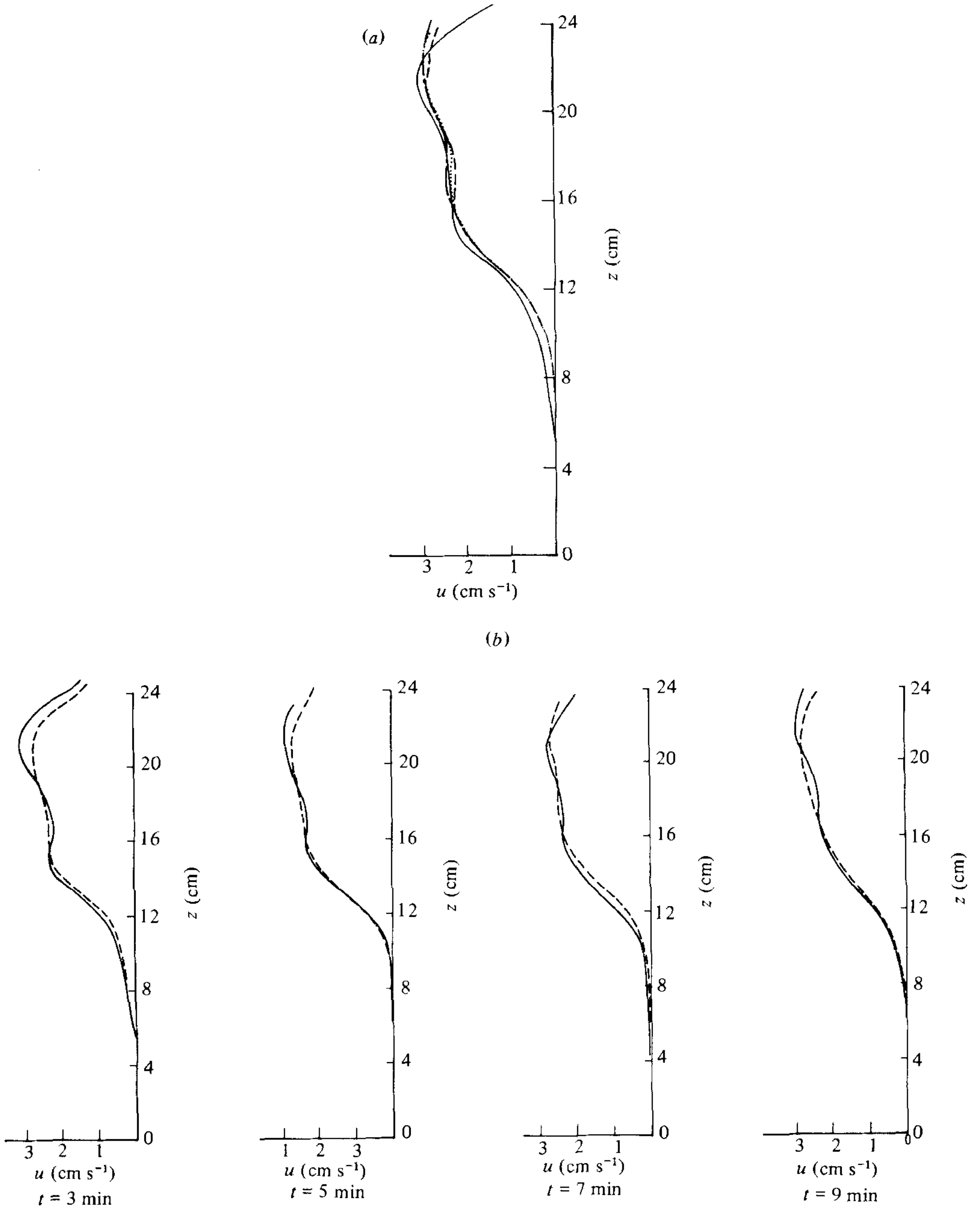

FIGURE 5. (*a*) Overlay of velocity profiles for the same run at four different elapsed times: —— 3 min; – – – 5 min; · · · · · 7 min; — · — 9 min. (*b*) Comparison of velocity profiles for two different runs at four values of elapsed time: —— initial run; – – – repeat run. (*c*) Spanwise velocity distribution made using hot-film probes positioned at three vertical locations. The high-frequency activity noted on these signals is due to the slight amount of wave motion on the free surface of the facility. —— traverse towards inner wall; – – – traverse towards outer wall.

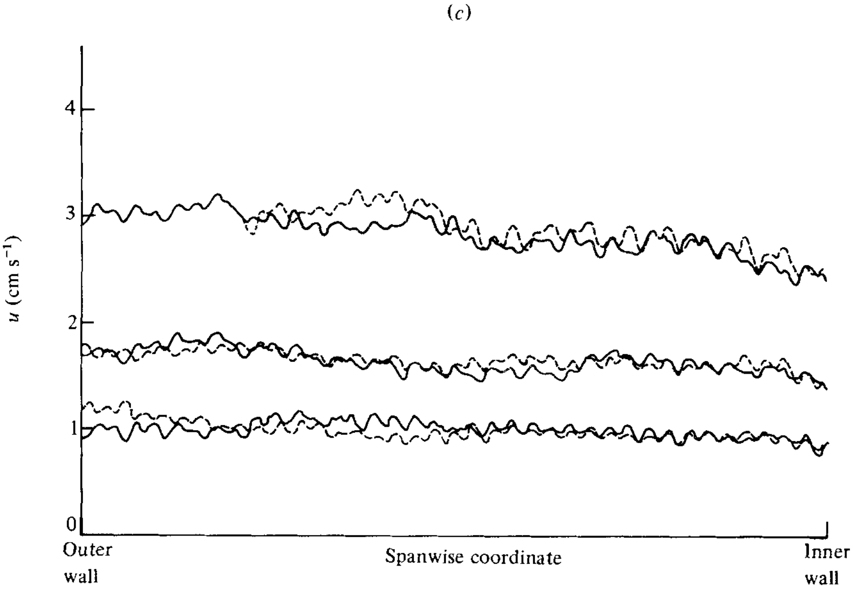

FIGURE 5(c). For legend see p. 352.

initial attempts to measure the velocity profile with a traversing hot-film probe yielded very poor results due to such difficulties as vibrations, nonlinear response, thermal variations in the ambient fluid and problems associated with measuring horizontal velocities with a probe that is moving in the vertical direction.†

The results of the velocity-profile measurements made using the bubble wire revealed that for typical operating conditions the characteristic thickness of the sheared region was on the order of 5–10 cm. For the experiments to be described this finite thickness associated with the sheared region was of crucial importance. We found, for example, that many of the interesting aspects of the internal-wave/mean-flow interaction occur in the neighbourhood of the critical layer. Had the critical layer been embedded in a region of large velocity and/or density gradient (e.g. a layered flow) it would have been difficult to differentiate between critical-layer effects and those associated with the large anomalies in the ambient medium.

In addition to the velocity profile, measurements were made of the vertical distribution of density using a conductivity probe. The nonlinear response of this sensor to saline variations was eliminated using a polynomial linearization circuit.

Finally, the internal waves generated by the various sources were visualized using the shadowgraph technique. The light source for these visualizations was a 100 W mercury lamp collimated using a 12 in. $f/8$ spherical mirror.

Before discussing the results of the experimental investigation, it is worth while to describe briefly some of the characteristics of the flow field generated by this new facility, so that one may have an appreciation for the type of experiments which can be performed in the apparatus. Of particular concern in the early stages of the study was determining the degree to which the shear flow was steady and repeatable. To

---

† Attempts to use a split-film probe to overcome the problem of vertical motion also proved fruitless, primarily due to the poor signal/noise characteristics of the differenced signal.

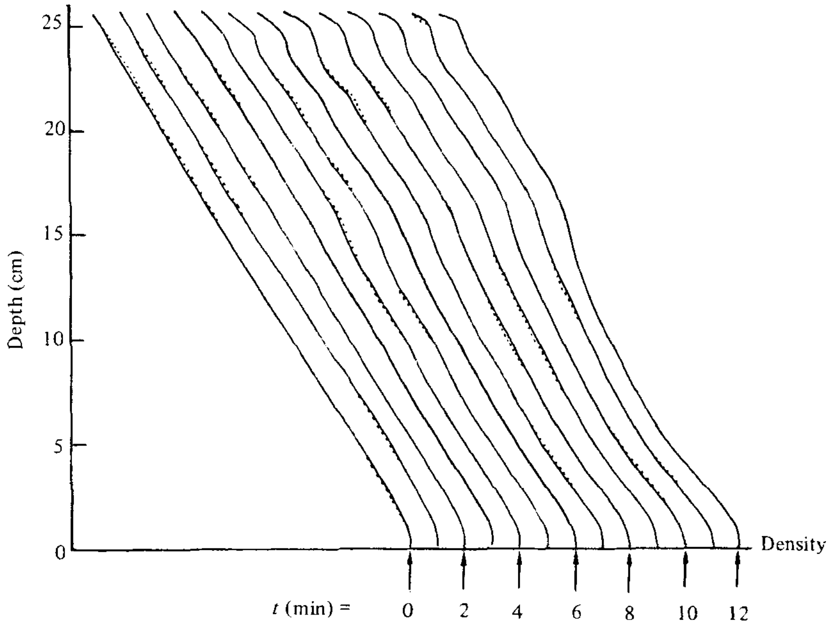

FIGURE 6. Evolution of the density profile. Distribution for $t = 0$ varies between $\rho = 1{\cdot}183$ at the bottom to $\rho = 1{\cdot}021$ at the top. Succeeding profiles offset by $\Delta\rho = 0{\cdot}061$. —— initial run; ····· repeat run.

study the transient nature of the flow field, several tests were performed to monitor the evolution of both the velocity and density profiles for running times of up to 10 min. Figure 4 shows the results of a series of velocity-profile measurements made at 12 s intervals for a running time slightly in excess of 10 min. These profiles were traced by hand from photographs of the hydrogen-bubble-wire images. One sees from these data that, after some initial period of transience (lasting roughly 1–2 min), the flow field achieves a relatively steady profile. Fluid velocities in the upper layer are typically about 2·5–3 cm s^{-1} (for this particular test condition) and the fluid in the lower layer is nearly quiescent (< 1 mm s^{-1}). Between the upper and lower regions of the tank is a shear layer having a characteristic thickness of about 5 cm and shear $\partial u/\partial z \simeq 0{\cdot}5\,\text{s}^{-1}$. The global Richardson number in this region is about $Ri = 25$. Figure 5(*a*), which presents an overlay of four profiles at elapsed times of 3, 5, 7 and 9 min, clearly demonstrates the high degree of steadiness over this running time. The repeatability of these profiles is exhibited in figure 5(*b*). Here the results of a repeat run, performed after the tank had been drained and refilled, are compared with those of the initial run. Although there is some degree of dissimilarity, the profiles are seen to agree reasonably well.

Figure 5(*c*) presents measurements of the cross-tank variation in the mean velocity, which were made at three vertical positions by slowly (approx. 1 mm s^{-1}) traversing hot-film probes laterally across the tank. To provide some measure of repeatability, two such traverses were made.† The probes were then calibrated by towing them through quiescent fluid at various velocities. The rather prominent high-frequency oscillatory behaviour noted in this figure is due to a slight amount of surface-wave

---

† During the second traverse a bubble attached itself to the uppermost probe, thus altering its calibration. This portion of the data has been deleted from the figure.

activity present in the tank. These surface waves are of extremely small amplitude (< 1 mm), but because of their long wavelengths (about 3–5 m) the wave-induced orbital velocities are appreciable. The most important feature to note in figure 5 (*c*) is the degree to which the mean horizontal velocity varies across the span of the test section. For the uppermost probe, we find that the centre-line velocity is about 2·9 cm s^{-1} and varies from 2·5 cm s^{-1} on the inside section of the annulus to about 3 cm s^{-1} on the outside. The lowest probe varies from about 0·85 cm s^{-1} to 1·1 cm s^{-1}. Although undesirable, such span-wise flow variations are an almost unavoidable feature of such an annular geometry. To put these variations in perspective, though, the span-wise gradient of velocity at its maximum is about 0·03 s^{-1}, which is an order of magnitude smaller than the vertical gradient of velocity, which is typically about 0·5 s^{-1}.

The corresponding evolution of the density profile, measured at 1 min intervals, is presented in figure 6, along with the results of a repeat run. One observes here that the initial linear density profile develops a slight bend in the centre of the channel after roughly 7 min of running. The cause of this change is believed to be due to the slight amount of mixing which occurs at the downstream exit of the pump (which is quickly suppressed by the buoyancy). It is significant to note, however, that the profile remains reasonably smooth throughout the duration of the test. Furthermore, most of the experiments to be described required only about 60–100 s to perform, and were usually completed within the first 5 min of running. We note, however, that such nonlinearity in the mean density profile could actually be beneficial in certain experiments where, for example, one might be interested in assessing the effects of vertical density structure on the wave field. Finally, one notes from figure 6 that the repeat run is almost indistinguishable from the initial run. Thus, at least in terms of the density profile, the flow field generated by this facility is quite repeatable from run to run.

3. Oscillating cylinder with shear

The first experiments to be discussed extend the work of Mowbray & Rarity (1967) to include the effects of shear. Essentially, the experimental configuration consisted of a circular cylinder (2·54 cm diameter) which spanned the test section and oscillated $\pm 0{\cdot}25$ cm horizontally at a constant frequency ranging between 0·20 and 0·33 Hz. The density profile for these tests is shown in figure 7, where it is seen that for the most part of the profile is linearly dependent upon depth (Brunt–Väisälä frequency, $N = 2{\cdot}49\ s^{-1}$), although near the top a sharp change in the gradient is observed.

Before presenting the results of these experiments it is worth while to discuss briefly the character of the wave patterns one would anticipate, based upon the theory of linear internal waves.† The vertical-mode structure of a linear internal wave in an inviscid stratified shear flow is govered by the Taylor–Goldstein equation which may be written as

$$\hat{w}_{zz}(z) + Q(z)\,\hat{w}(z) = 0, \qquad (1)$$

---

† The simple analysis presented here basically follows that given by Phillips (1966), with the exception that shear is introduced.

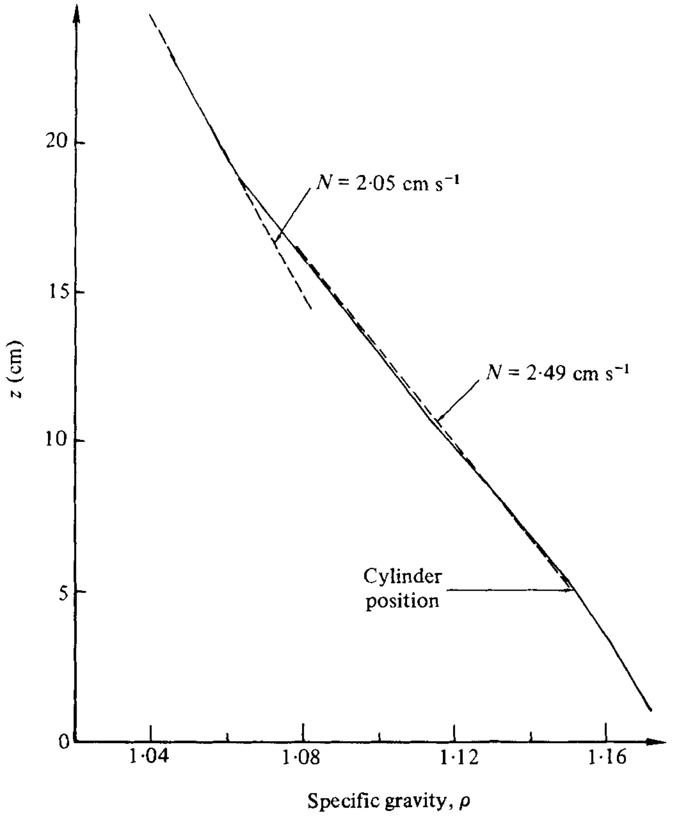

FIGURE 7. Measured density profile for oscillating-cylinder experiments.

where

$$Q(z) = k_x^2\left[\frac{N^2(z)}{(\omega \pm \bar{U}(z)\,k_x)^2} - 1\right] - \left[\frac{k_x\bar{U}_{zz}(z)}{U(z)\,k_x \pm \omega}\right],$$

$$N^2(z) = \frac{-g}{\rho}\frac{\partial\rho}{\partial z},$$

and the vertical velocity is assumed to have the form

$$w(x,z,t) = \hat{w}(z)\,e^{i(k_x x \pm \omega t)} + \text{c.c.}$$

The ± notation in the above expression is introduced in order to distinguish between waves travelling in the positive or negative direction.

If $Q(z)$ is assumed to be a slowly varying function, then the WKB approximation is valid and the solution of equation (1) is given by

$$\hat{w}(z) = \frac{A}{Q(z)^{\frac{1}{4}}}e^{i\theta(z)} + \frac{B}{Q(z)^{\frac{1}{4}}}e^{-i\theta(z)}, \tag{2}$$

where $\theta(z)$ is the phase function. A vertical wavenumber k_z may be defined as

$$k_z(z) \equiv \frac{d\theta}{dz} = k_x\left[\frac{N(z)^2}{(\omega - \mathbf{U}.\mathbf{k})^2} + \frac{U_{zz}}{k_x(\omega - \mathbf{U}.\mathbf{k})} - 1\right]^{\frac{1}{2}}, \tag{3}$$

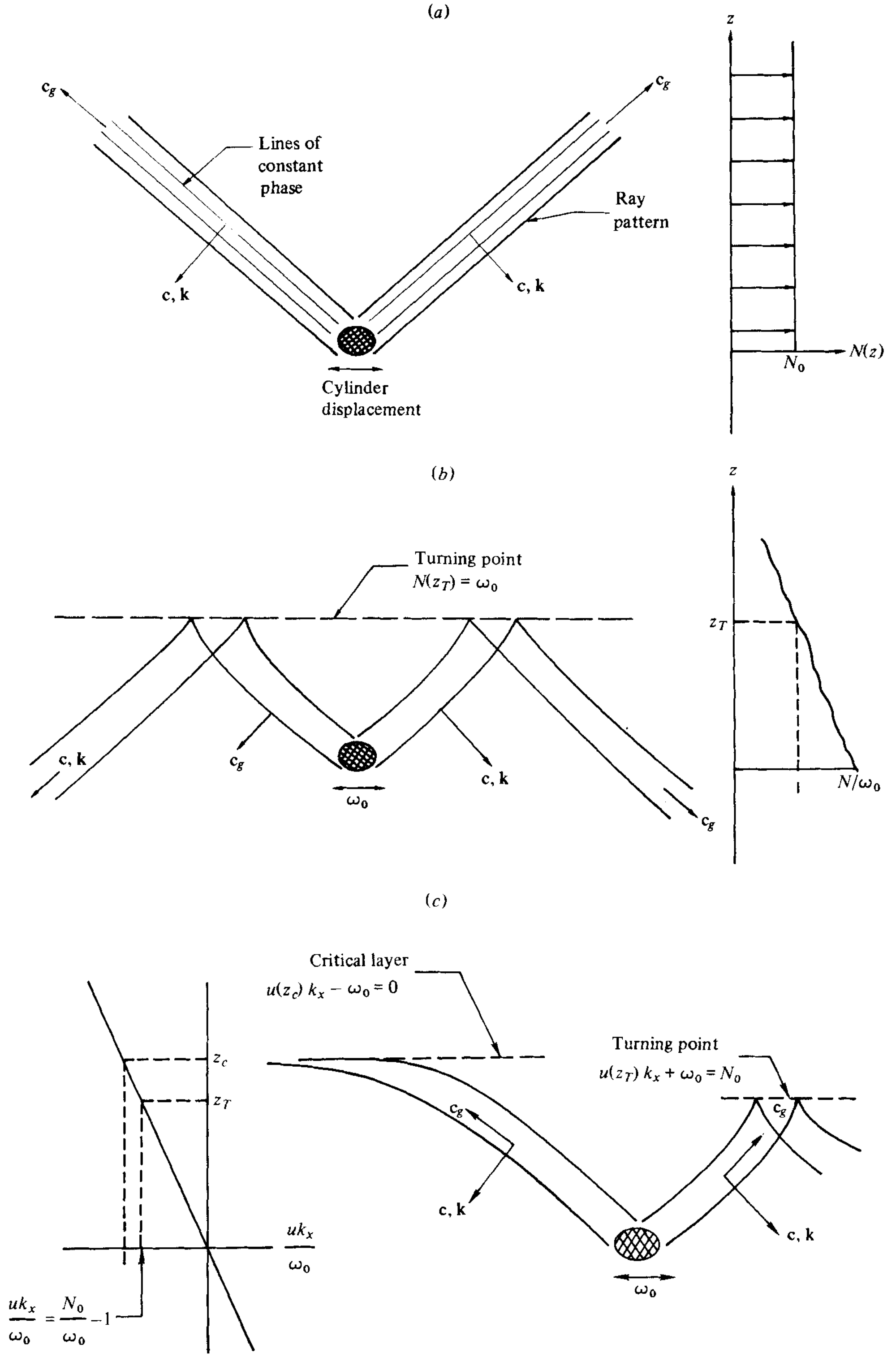

FIGURE 8. Schematic representations of the ray patterns generated by an oscillatory cylinder: (*a*) in an unsheared constant-N fluid; (*b*) in an unsheared fluid with variable Brunt–Väisälä frequency; (*c*) in a shear flow with constant Brunt–Väisälä frequency.

where vector notation for the wavenumber and mean flow velocity has been introduced. This solution is valid provided that

$$\frac{d}{dz}k_z^{-1} \ll 1.$$

The dispersion relation, given by equation (3), may be used to trace the ray patterns generated by the oscillating cylinder. Several cases are considered.†

Case A: $\overline{U} = 0, N = \text{const.} = N_0$. This is the case discussed in detail by Mowbray & Rarity (1967). The dispersion relation is given by the well known expression

$$\frac{\omega}{N_0} = \frac{k_x}{(k_x^2+k_z^2)^{\frac{1}{2}}} = \sin\theta, \tag{4}$$

where θ is the angle between the wave ray and the horizontal. The ray pattern for this case is illustrated schematically in figure 8(*a*). Note that for $\omega \ll N_0$ the group velocity is almost horizontal, but rotates towards the vertical as $\omega \rightarrow N_0$.

Case B: $\overline{U} = 0, N \neq \text{const.}, \omega = \text{const.} = \omega_0$. The dispersion relation for this case is given by

$$k_z = k_x\left[\frac{N^2(z)}{\omega_0^2} - 1\right]^{\frac{1}{2}} \tag{5}$$

and the ray pattern is shown schematically in figure 8(*b*). Note that at the turning point z_T, defined by $N(z = z_T) = \omega_0$, the wavenumber vector becomes horizontal and the WKB solution given by equation (2) has a weak singularity. However, as noted by Phillips (1966), formulating the WKB solution in the neighbourhood of z_T (given in terms of Airy functions) reveals that within the WKB approximation total reflection occurs at the turning point.

Case C: $N = \text{const.} = N_0, \omega = \text{const.} = \omega_0, \overline{U}(z) \neq \text{const.}, \overline{U}_{zz} = 0$. For this case, the dispersion relation is given by

$$k_z = k_x\left[\frac{N_0^2}{(\omega_0 - \mathbf{U}.\mathbf{k})^2}\right]^{\frac{1}{2}}, \tag{6}$$

where one must now distinguish between waves propagating with or against the mean current $\overline{U}(z)$. For waves propagating with the current, a critical layer exists at z_c, defined by $\overline{U}(z = z_c)\,k_x = \omega_0$. At this point the WKB analysis breaks down, as the Taylor–Goldstein equation becomes singular, and to proceed further one needs to reformulate the problem. However, we note that, as the ray *approaches* the critical level, k_z becomes much greater than k_x and the group velocity becomes nearly horizontal. For waves propagating against the current, a turning point exists at

$$\omega_0 + \overline{U}(z_T)\,k_x = N_0.$$

As previously noted, the solution in the neighbourhood of this point is given in terms of Airy functions, and one can show that the wave totally reflects. It is important to recognize, however, that in this case the waves reflect due to the presence of the

---

† We note here that, in general, the oscillating cylinder excites a continuum of wavenumbers. For conceptual simplicity, however, we will assume that the energy-containing portion of the spectrum may be characterized by a single dominant wavenumber k_x (experimentally, one can typically discern only one line of constant phase per oscillation, thus supporting this conceptualization). It is felt that this approximation is consistent with the degree of rigour for which this qualitative discussion is intended.

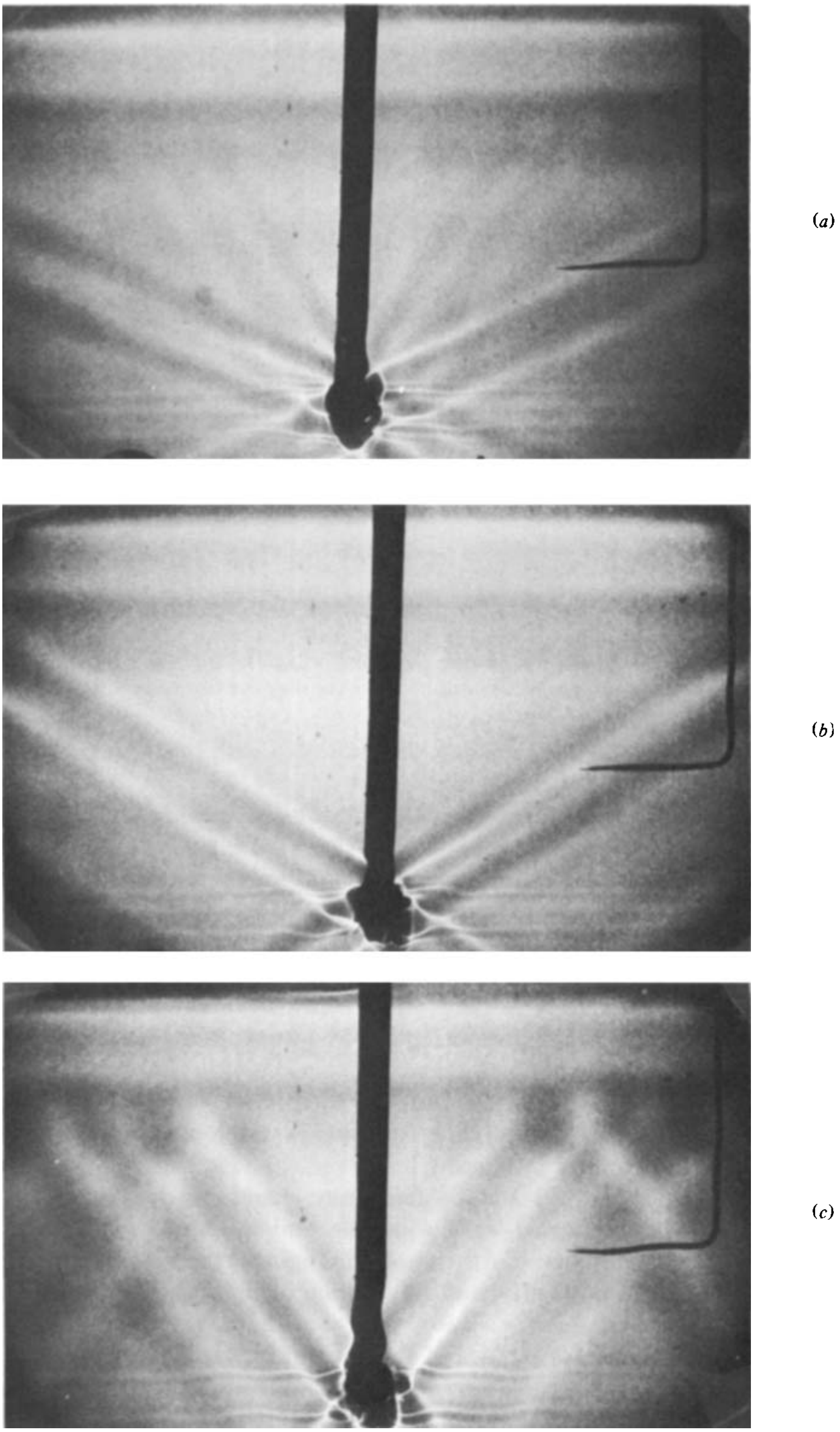

Figure 9. Experimentally observed ray patterns generated by an oscillating cylinder in an unsheared fluid. The density distribution for these runs is shown in figure 7. (*a*) $\omega/N_0 = 0{\cdot}40$; (*b*) $\omega/N_0 = 0{\cdot}52$; (*c*) $\omega/N_0 = 0{\cdot}82$.

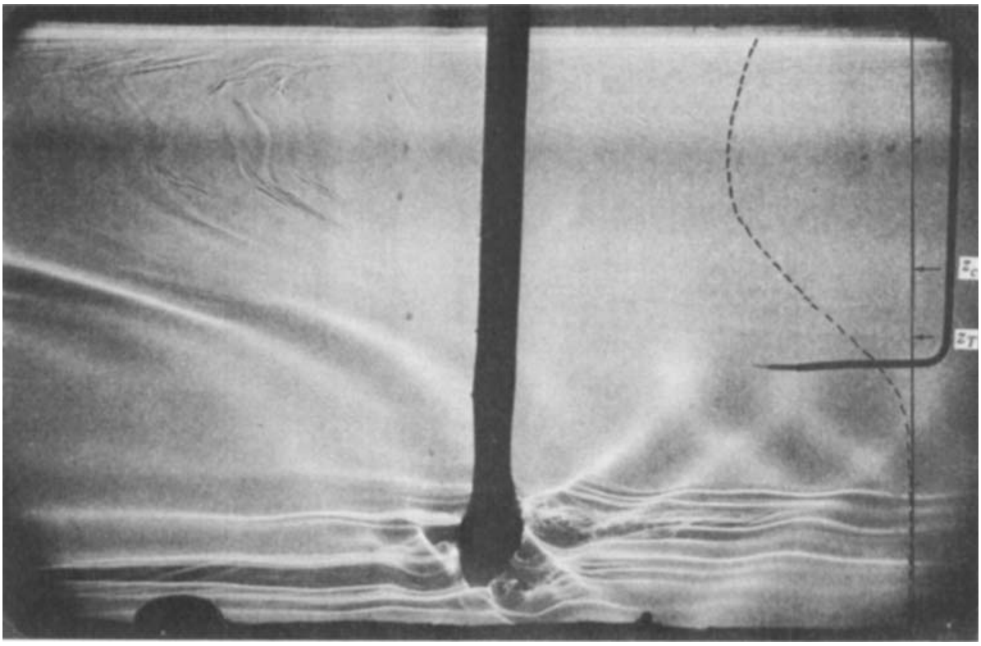

FIGURE 10. Experimentally observed ray pattern generated by an oscillating cylinder in a shear flow. The corresponding velocity profile, measured using the hydrogen-bubble wire, is shown superimposed on the photograph. Maximum fluid velocity for this case is 1·65 cm s^{-1}.

mean shear rather than due to anomalies associated with the density structure. Both of these situations are depicted in figure 8(*c*).

The results of the experimentally observed wave patterns generated by an oscillating cylinder are presented in figures 9 and 10. Figure 9 shows the results of three experiments, performed in quiescent fluid, which merely repeat the Mowbray & Rarity (1967) experiment. The ray pattern for the case $\omega/N_0 = 0{\cdot}40$ is shown in figure 9(*a*). Here, the rays look qualitatively similar to the anticipated pattern (figure 8(*a*)), with internal-wave energy being ducted along the characteristic trajectories defined by equation (4). One also notes the faint presence of the ray pattern associated with the first harmonic of the cylinder oscillation frequency. This contribution disappears, however, when $\omega/N_0 > 0{\cdot}50$ (such that the frequency of the harmonic is greater than N_0), as demonstrated in figure 9(*b*). Finally, figure 9(*c*) shows the case $\omega/N_0 = 0{\cdot}82$, where one observes that a reflection occurs close to the top. Reference to the density profile for this case shown in figure 7 reveals that above this point $\omega/N > 1$. Thus, the point where the Brunt–Väisälä frequency changes in magnitude represents a turning point in the internal-wave equation, and the anticipated wave reflection (figure 8(*b*)) is clearly observed. Also seen in this figure is the wave ray emanating from below the cylinder which reflects off the bottom of the channel, propagates upward through the medium and reflects a second time at the turning point.

Figure 10 shows the appearance of the wave field when shear is present. In this figure, the fluid is moving from right to left, with the upper layer moving faster than the lower layer. The velocity profile obtained simultaneously from the hydrogen-bubble wire is superimposed upon the figure. For this case the maximum fluid velocity is 1·65 cm s^{-1}. The cylinder oscillation frequency is $\omega/N_0 = 0{\cdot}70$ and the horizontal phase speed is 1·1 cm s^{-1}. As anticipated from the linear dispersion relation, one sees that the waves propagating in the same direction as the fluid motion become elongated by the shear and are absorbed into the mean flow close to the measured position of the critical level (denoted by an arrow in the velocity profile). The waves propagating against the current are observed to reflect at the position of the turning point (also marked by an arrow). In general, the ray pattern looks remarkably similar to that anticipated from the linear internal wave theory (figure 8 (*c*)).

4. Critical-level flows

4.1. *Background*

In § 3, preliminary experiments were described which dealt qualitatively with the effects of shear on propagating internal waves. These results were interpreted in terms of steady-state, linear, inviscid internal-wave theory. However, many of the difficult details of the problem related to the presence of time-dependent viscous and nonlinear critical-level flows have not been incorporated into the analysis. In the present section we will consider in somewhat more detail the dynamic interaction which occurs between an internal-wave field and a steady shearing motion in the presence of a critical layer.

The effect of a critical layer upon a monochromatic disturbance has been investigated in detail by Booker & Bretherton (1967). Their analysis, which can best be described as a linear, unsteady, inviscid initial-value problem, reveals that for Richardson numbers of order unity or greater the critical layer represents a nearly impenetrable barrier to incoming waves. The attenuation of wave-action flux across the critical layer is $\exp(2\phi\mu)$, where $\mu = (Ri-\frac{1}{4})^{\frac{1}{2}}$, Ri is the Richardson number and ϕ is commonly referred to as the 'phase change'. For the linear, inviscid, unsteady problem $\phi = -\pi$, so that even for moderate values of Ri significant attenuation occurs across the critical layer. The interaction of the wave field with the critical layer results in a transfer of momentum flux from the wave to the mean flow, a process commonly known as critical-layer absorption. It is significant, however, that within the neighbourhood of the critical layer the Booker–Bretherton analysis is asymptotically singular, with wave-induced horizontal velocity perturbations increasing without bound as $t^{\frac{1}{2}}$. This result is due to the simultaneous neglect of nonlinear, viscous and diffusive terms in the governing equations. It is clear, however, that for an inviscid fluid as the velocity grows in time nonlinear effects must ultimately become manifest. From the Booker–Bretherton analysis one finds that this occurs on a time scale given by

$$t_{NL} = O(k_x^{-\frac{2}{3}}\,U_z^{-\frac{1}{3}}\,w_0^{-\frac{2}{3}}),$$

where U_z measures the mean shear, k_x is the horizontal wavenumber and w_0 is the characteristic vertical velocity of the wave forcing. If the fluid is slightly viscous then the viscous terms in the neighbourhood of the critical level become comparable with the linear inviscid terms on a time scale given by

$$t_v = O(k_x^{-\frac{2}{3}}\,\nu^{-\frac{1}{3}}\,U_z^{-\frac{2}{3}}),$$

where ν is the kinematic viscosity. The ratio of these two quantities is

$$\frac{t_{NL}}{t_v} = \left(\frac{\nu U_z}{u_0^2}\right)^{\frac{1}{3}} \equiv \lambda, \tag{7}$$

which is the λ parameter discussed by Maslowe (1972). The long-time evolution of the flow in the neighbourhood of the critical layer will depend crucially upon the order of λ.

When $\lambda \gg 1$ the time required for the viscous terms to be comparable with the linear inviscid terms is short relative to the time required for the onset of nonlinear effects. Hazel (1967) has shown for the steady state, linear, viscous problem that the phase change across the critical layer is the same as that for the inviscid, unsteady case, *viz* $-\pi$. Hazel also found that negligible wave reflection occurred at the critical layer. Consequently, in this limit one might expect that for early times the critical layer acts to attenuate wave energy proportional to $\exp(-2\mu\pi)$, consistent with the Booker–Bretherton analysis, and continues to do so for larger times, consistent with Hazel's results. Whether or not nonlinearity ever becomes important in this limit is uncertain. It is conceivable, however, that, if λ is very large, viscous dissipation could suppress entirely the $t^{\frac{1}{2}}$ growth of the horizontal velocity perturbation. In this case virtually none of the incoming wave action (for moderate values of Ri) would be transmitted or reflected at the critical layer for all time. Instead, the wave-momentum flux would be absorbed into the mean flow through the gradient of the Reynolds stress, as discussed by Jones & Houghton (1971).

The degree to which viscosity is capable of suppressing one form of nonlinear behaviour, *viz* that of convective instability (i.e. wave overturning), has been discussed by Fritts & Geller (1976). Using as a criterion of incipient breaking the point where the vertical gradient of the density is zero (equivalent to the velocity criterion of Orlanski & Bryan (1969)), they show that convective overturning in the neighbourhood of the critical layer is stabilized by viscosity provided $z_c < \beta z_\nu$, where

$$z_c \equiv \left(\frac{Ri\, w_0^2}{U_z C k_x^2}\right)^{\frac{1}{3}}, \quad z_\nu \equiv \beta\left(\frac{\nu}{k_x U_z}\right)^{\frac{1}{3}}. \tag{8}$$

Here, C is the wave phase speed, w_0 the vertical velocity at the edge of the shear region, and β an $O(1)$ constant. The implication of this viscous-stability criterion is that for sufficiently strong dissipation the absorption of incoming-wave momentum flux into the mean flow proceeds by laminar processes. For weak dissipation, however, z_c may exceed z_ν and convective instability and turbulent motions may develop near the critical level, requiring the inclusion of nonlinear effects for an accurate description of the flow field.

In the limit $\lambda \ll 1$, the $t^{\frac{1}{2}}$ growth of the horizontal velocity perturbation leads to a manifestation of the nonlinear effects prior to the point in time when they are suppressed by viscosity. The character of the flow field in this limit is extremely complex, and most of the work which has been done on this subject involves numerical computations. A notable exception, however, is the recent work of Brown & Stewartson (1980) who consider the first effects of weak nonlinearity upon the transient critical-layer problem forced by an internal gravity wave maintained a finite distance away. Their approach involves an expansion in powers of the nonlinear time scale $\epsilon^{\frac{2}{3}}(U_z t)$, where ϵ measures the strength of the forcing. An important result of this analysis is that in the high-Richardson-number limit the inclusion of weak nonlinearity has virtually no effect upon the transmissivity of the critical layer, but that the reflected wave is larger by a factor of $\exp(\mu\pi)/\mu$ than that obtained from the linear analysis. Unfortunately, due to the extreme complexity of the analysis, only the first harmonic of the forcing disturbance could be computed. This implicitly limits the temporal domain over which the solution is valid. Numerical solutions for larger time (to be discussed) exhibit the excitation of many harmonics in the critical layer.

That nonlinearity in the critical-layer region can lead to wave reflection has been demonstrated numerically by Breeding (1971). These calculations show that such reflections become significant as the Richardson number decreases, being about 35 % of the incident wave energy for $Ri \simeq 0{\cdot}5$ (cf. 4 % for linear waves). For all cases considered, the amplitude of the transmitted wave was $O(e^{-\mu\pi})$ or less. Not observed in Breeding's calculations, however, was any evidence of convective instability or turbulent breakdown in the critical layer, even though the viscous stability criterion of Fritts & Geller (1976) is violated for some cases. Geller, Tanaka & Fritts (1975) suggest that this is due to Breeding's use of a rather large eddy viscosity for computational purposes, which effectively suppresses the growth of such instabilities. The more recent calculations of Fritts (1979) do indeed show that nonlinearity and transience permit the excitation and growth of small-scale disturbances which may be propagating and/or vertically evanescent above and below the critical layer. The process may be quite complex, however, as the propagating modes carry wave action away from the critical layer while the evanescent modes (Kelvin–Helmholtz instabilities) are able to extract excess energy and stabilize the shears created by the incident waves. As the Kelvin–Helmholtz waves achieve significant amplitude, nonlinear wave–wave interactions among these modes produce large perturbations in the lower harmonics which may excite additional radiating waves (Fritts 1979).

All of the above nonlinear internal-wave theories are in qualitative agreement with the corresponding work which has been done on nonlinear time-dependent Rossby waves. In particular, Stewartson (1978) and Warn & Warn (1978) have demonstrated analytically the growth of harmonics in the critical layer due to nonlinear interactions, and have shown that the phase change across the critical layer varies on the nonlinear time scale $\epsilon^{\frac{1}{2}}(U_z t)$. Initially, the phase shift is $-\pi$, consistent with linear theory (Dickenson 1970), but varies significantly (and at certain stages is positive, indicative of over-reflection) when the nonlinear time scale is $O(1)$. At this point, the wave field is populated by many harmonics which become as energetic as the primary wave itself and effect *global* changes (as opposed to changes confined to the critical-level region) in the character of the flow field. These inviscid theories, however, never achieve a steady state. As time progresses the harmonic-generation process continues and higher and higher oscillation frequencies evolve. This result would almost certainly be modified by the inclusion of viscosity. The numerical computations of Beland (1978), for example, which include viscous dissipation, show agreement with the inviscid nonlinear theories for early times, but demonstrate that on a viscous time scale the harmonic generation is ultimately suppressed by viscosity. Asymptotically, the steady-state solution of Haberman (1972) is approached.

4.2. *Critical-layer experiments*

The preceding concepts provided the motivation for a series of experiments designed to study under controlled laboratory conditions what roles nonlinearity, viscosity and transience play in the interaction of an internal gravity wave with a steady shearing motion. The approach taken is of a 'first-look' nature and most of the results are fairly qualitative, being presented in the form of shadowgraph images of the wave

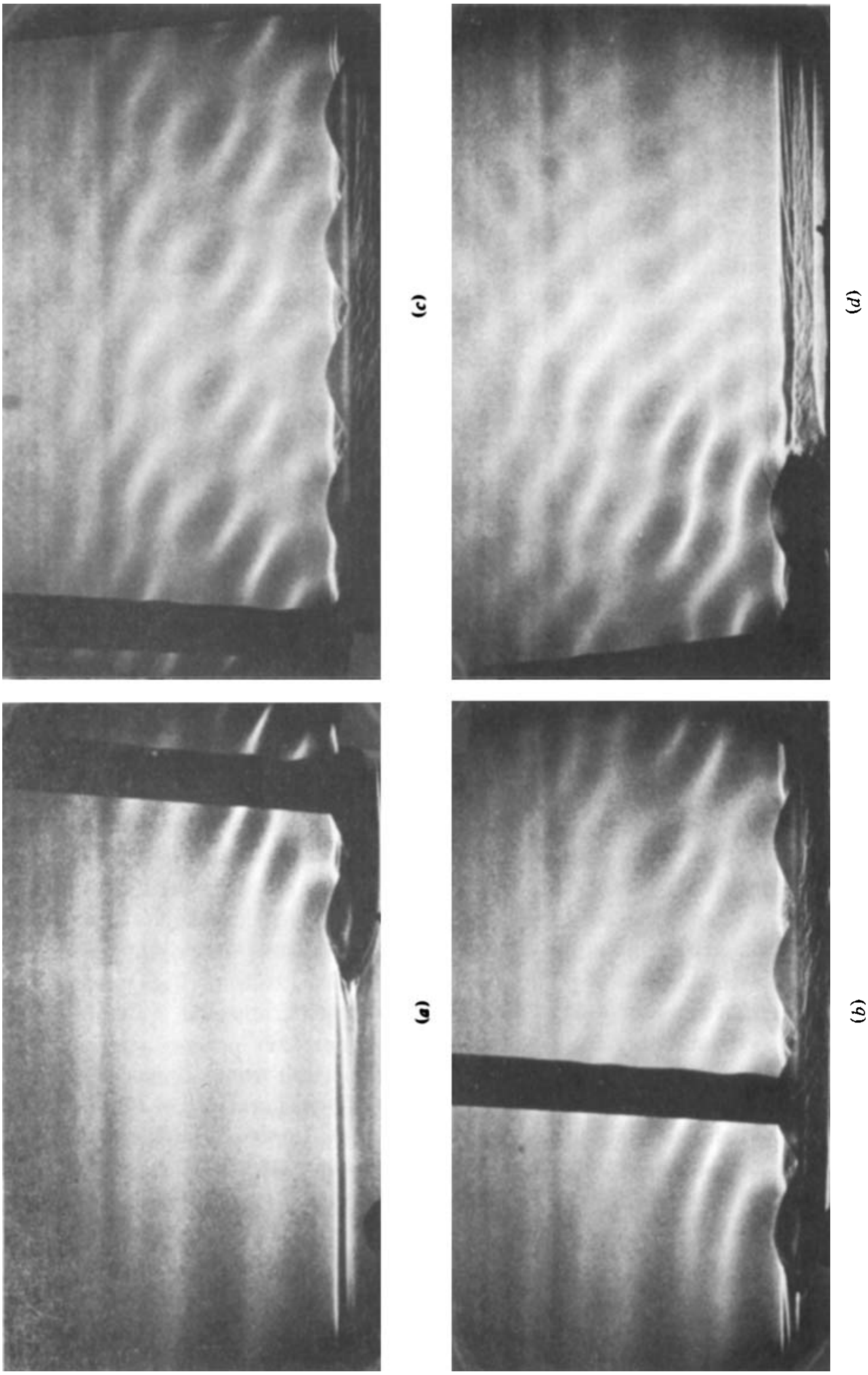

FIGURE 11. Wave pattern generated by wavy boundary moving through quiescent fluid. Towing speed is $1{\cdot}12\ \mathrm{cm\ s^{-1}}$.

field. Of specific interest in these experiments was whether any evidence of nonlinearity could be observed in the form of wave transmission or reflection at the critical layer, harmonic generation or global changes to the mean flow. It was also of interest to see under what conditions convective instabilities develop at the critical layer, and whether Kelvin–Helmholtz wave growth and subsequent turbulent breakdown leads to unsteady wave radiation.

Two wave sources were used for these experiments. The first internal-wave generator was a sinusoidally corrugated boundary having a wavelength of 7·62 cm, a peak–peak amplitude of 1·27 cm and an overall length of 61 cm (i.e. 8 wavelengths). The wavy boundary was positioned 2·54 cm above the bottom of the channel. This internal-wave source was used to model the generation of an internal-wave train that is nearly monochromatic, and of large spatial extent; i.e. the experimental analogue of the configuration considered by Booker & Bretherton (1967). The second internal-wave source was a circular cylinder having a diameter of 2·65 cm, mounted with its axis in the span-wise direction 5 cm above the bottom of the tank. The cylinder represents an internal-wave forcing which is broad-banded and spatially compact.

Internal waves were generated by towing these objects through the test section in the same direction as the fluid motion. For constant towing speed (excluding start-up transients) the excited wave field is steady in a frame of reference moving with the object. In laboratory co-ordinates, these waves propagate at the towing speed. For most of the experiments the fluid in the lower portion of the tank was kept nearly quiescent (< 1 mm s^{-1}) and achieved a maximum velocity of 1·5–4·5 cm s^{-1} somewhere above the centre. By adjusting the towing speed such that it was greater than zero but less than the maximum fluid velocity, somewhere in the tank the local fluid velocity was equal to the internal-wave phase speed, and a critical layer existed. Similarly, the existence of a critical layer could be avoided by requiring the towing speed to exceed the maximum fluid velocity.

Figure 11 shows the wave field generated by the corrugated boundary with the ambient fluid in a quiescent state. Here, the boundary is moving from right to left at a speed of 1·12 cm s^{-1}. In figure 11(*a*) the boundary has just reached the observation point, which is 75 cm from the end of the test section. The light and dark regions in the shadowgraph image represent the lines of constant phase of the wave motion. One sees here a ray pattern inclined at roughly 30° relative to the horizontal and propagating downstream with a phase speed equal to the towing velocity. In examining figure 11 one finds that along the boundary within the troughs recirculation regions exist, presumably as a result of flow separation off the lee side of the wave. This was an unfortunate result. In order to promote the generation of large-amplitude waves, with the hope of observing nonlinear effects, the wavy boundary was deliberately designed with a rather steep wave slope ($ka \simeq 0{\cdot}52$). The presence of recirculation regions, however, effectively diminished the amplitudes of the waves generated by the body. Moreover, the wave field generated by the boundary was not purely monochromatic, although a dominant wavelength equal to the corrugation wavelength still existed. One also sees a change in the character of the wave field near the end of the body (figure 11(*d*)) due to end effects.

Figure 12 presents the appearance of the wave field when the shear is turned on and a critical layer exists in the flow (the measured velocity profile is superimposed on figure 12(*a*)). The flow is from right to left in this figure, and the maximum fluid

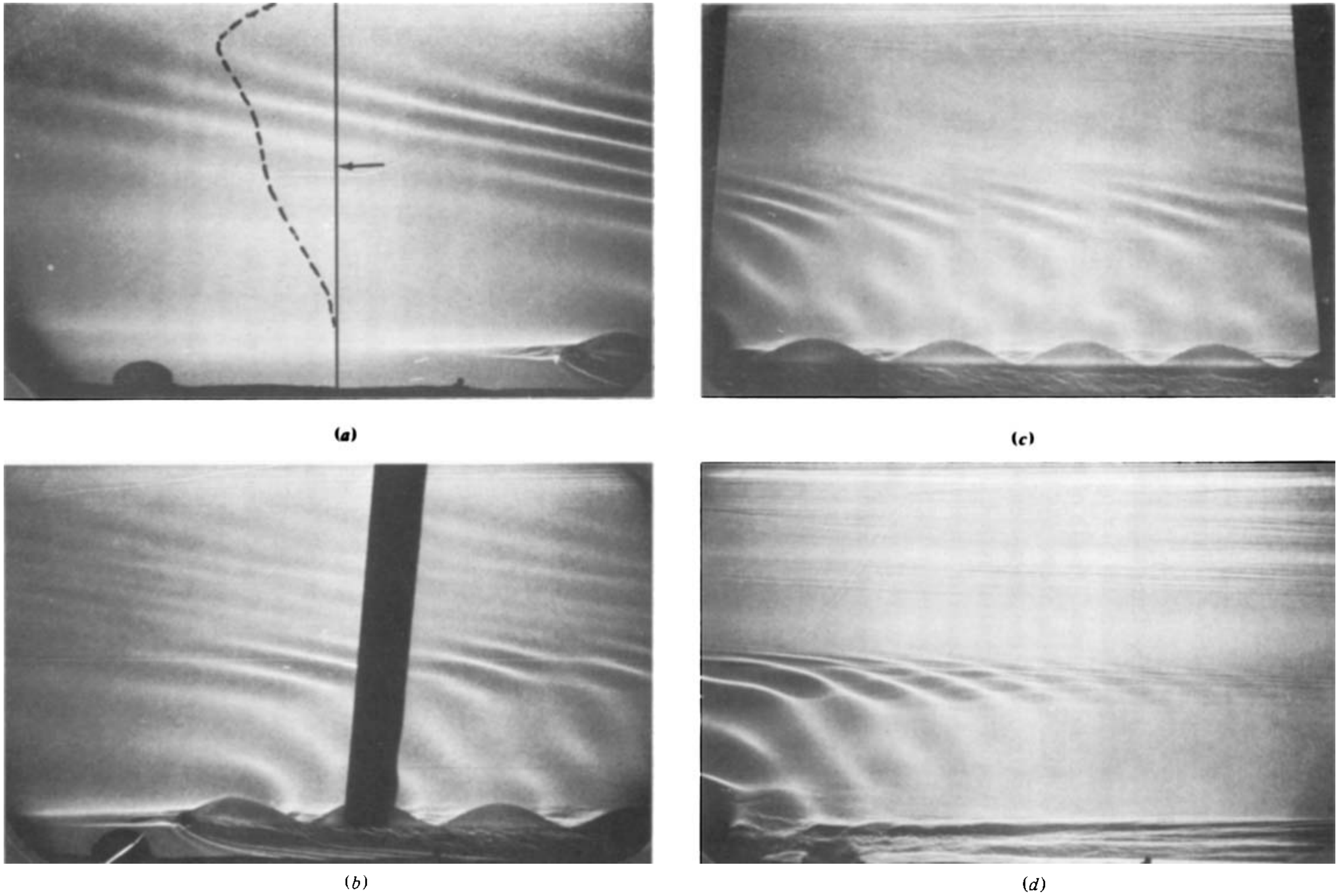
(a) (c) (b) (d)

FIGURE 12. Wave pattern generated by wavy boundary moving through a shear flow when a critical layer exists. Measured velocity profile is shown superimposed on (a). Maximum fluid velocity is 1·79 cm s^{-1} and towing speed is 1·12 cm. Arrow denotes measured position of critical layer.

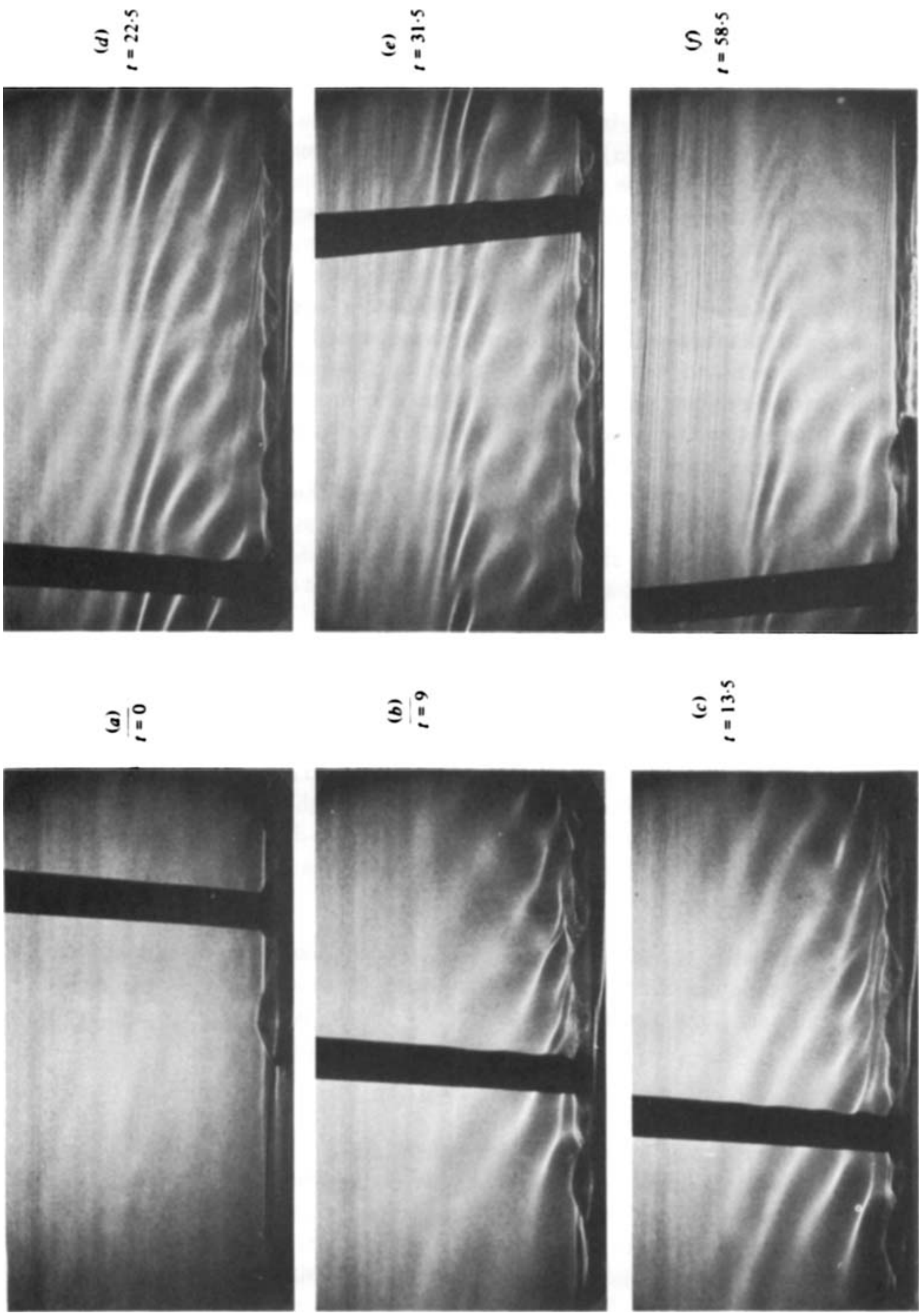

FIGURE 13. Wave pattern generated by wavy boundary in a shear flow during start-up transient. Elapsed times since impulsive start are: (*a*) $t = 0$ s; (*b*) $t = 9$ s; (*c*) $t = 15{\cdot}3$ s; (*d*) $t = 22{\cdot}5$ s; (*e*) $t = 31{\cdot}5$ s; (*f*) $t = 58{\cdot}5$ s.

velocity is $1{\cdot}79$ cm s^{-1}. The towing speed is $1{\cdot}12$ cm s^{-1}, and the measured position of the critical layer is denoted by an arrow in figure 12(*a*). The global Richardson number for this case, defined as $Ri = N_0^2 h^2/U_c^2$ (where N_0 is the ambient Brunt–Väisälä frequency, U_c the critical-layer velocity, and h the shear-layer half-thickness) is about $Ri = 319$. In figure 12(*a*), the boundary has just reached the observation station, and one observes a wave pattern which does not appear to be trapped, but rather extends above the position of the critical layer. These waves are believed to be due to transients associated with the start-up process, as evidenced by the results shown in figure 13. Here the wave field generated by the boundary immediately after the activation of the towing system is presented. One sees here that as the boundary is impulsively started a broad-band disturbance is generated which is *not* steady in a reference frame moving with the body. As noted by Booker & Bretherton (1967), these transient waves either radiate away to infinity or are absorbed into the shear flow, each at the critical layer associated with their frequency. The steady-state pattern which emerges is shown in figure 13(*e*).

Returning to an examination of figure 12, one sees that the steady (in body-fixed co-ordinates) wave field which develops is elongated by the shear in the neighbourhood of the critical layer. Figure 12(*c*) shows the upper half of the tank to be almost devoid of any wave motion, indicating that the degree of transmission of wave action through the critical layer is negligible. There is no obvious evidence of wave reflection or harmonic generation at the critical layer, nor is there wave overturning or turbulent breakdown. Whether or not these observations are consistent with our previous discussion depends upon the duration of the forcing and the value of the λ parameter.

From scaling the photographs, we estimate that the peak–peak isopycnic displacement excited by the corrugated boundary is about $0{\cdot}17$ cm. The shear in the critical-layer region is roughly $0{\cdot}14\ \mathrm{s}^{-1}$, and the time elapsed since the impulsive start-up is 113 s. Thus, the value of the quantity $\epsilon^{\frac{2}{3}} U_z t$, i.e. the non-dimensional time scale measuring the onset of nonlinear effects (Stewartson 1980), is

$$\epsilon^{\frac{2}{3}} U_z t \simeq 2{\cdot}7.$$

As this is of order unity, we conclude that sufficient time has elapsed for nonlinear effects to have become manifest. However, computing the relative magnitude of the viscous and nonlinear time scales, as measured by the λ parameter, we find from equation (7)

$$\lambda = \left(\frac{\nu U_z}{w_0^2}\right)^{\frac{1}{3}} \simeq 0{\cdot}63 = O(1).$$

As λ is of order unity, the conclusion one draws from these order-of-magnitude estimates is that in the experiments sufficient time has elapsed for nonlinearity to be of importance, but that the effects of *both* nonlinearity and viscosity become manifest at approximately the same time. This makes the interpretation of the experimental results within a theoretical framework somewhat difficult, since the two effects are in a sense oppositely directed. As previously noted, nonlinearity acts to promote energy transfer away from the critical layer through the generation of harmonics, and viscosity acts to suppress this harmonic generation and maintain the $-\pi$ phase shift. The combined problem where both nonlinearity *and* viscosity are important in a transient critical layer has not as yet been analysed theoretically, nor has it been fully explored numerically.

The lack of any discernible turbulent motions in the critical-layer region of figure 12 suggests that for these experimental test conditions the viscous stability criterion of Fritts & Geller (1976) should be satisfied. However, using the previous estimates for the isopycnic displacement and level of mean shear, one finds from equation (8) that

$$z_c = 2{\cdot}8\ \mathrm{cm}, \quad z_\nu = 0{\cdot}45\ \mathrm{cm}.$$

As z_c is significantly greater than z_ν, one would expect the critical-layer region to exhibit some degree of convective overturning and turbulent motions. That such turbulence is not observed experimentally is believed to be due to the manner in which the viscous effects are accounted for in the stability criterion. We herein propose an alternative viscous-stability criterion, based upon a wave-action approach, which appears to yield much better agreement with the experimental observations.

The wave-action theory, as derived by Bretherton (1966), has been modified to allow for weak dissipation (Grimshaw 1974; Redekopp, private communication). The resulting expression is given by

$$\frac{\partial}{\partial t}\left(\frac{\xi}{\omega'}\right) + \nabla . \mathbf{C}_g\left(\frac{\xi}{\omega'}\right) = -\nu|\mathbf{k}|^2\frac{\xi}{\omega'}, \tag{9}$$

$$\omega = \omega' + \mathbf{U}.\mathbf{k}, \quad \mathbf{k} = k_x\hat{\mathbf{x}} + k_z(z)\,\hat{\mathbf{z}},$$

where, to within the WKB approximation,

$$\omega' = \frac{N(z)\,k_x}{(k_x^2 + k_z^2(z))^{\frac{1}{2}}}, \quad \xi = \tfrac{1}{2}\rho_0\frac{w^2(z)\,N^2}{\omega'^2}. \tag{10}$$

From wave kinematics, one has

$$\frac{\partial k_z}{\partial t} + (\mathbf{C}_g . \nabla)\,k_z = k_z\frac{\partial U}{\partial z}. \tag{11}$$

Assuming the flow to be steady (in body-fixed co-ordinates) equations (9)–(11) may be integrated, and as a criterion for convective instability we may search for the point Z_c where the local density gradient is zero. For $Ri \gg 1$, this occurs where

$$Z_c \exp\left[\phi(Z_c)\right] = \left[\frac{Ri^{\frac{1}{2}}\,k_{z_0}w_0^2}{U_z^2\,k_x^2}\right]^{\frac{1}{3}}, \tag{12}$$

$$\phi(Z_c) = \frac{1}{9}\frac{Ri^{\frac{3}{2}}}{R_\nu}\left[\frac{1}{(Z_c/H_1)^3} - 1\right], \quad R_\nu \equiv \frac{k_x C^3}{\nu U_z^2}, \quad H_1 = C/U_z,$$

where for simplicity we have assumed a piecewise linear distribution for the mean velocity field. C is the wave phase speed (equal to the towing velocity), and the subscript '0' refers to conditions at the edge of the shear region.

Although the above model is only a crude approximation to the experimental conditions (more precise comparisons could be made using numerical solutions), it is of interest to see how well the above criterion predicts the experimental results. Again using the aforementioned estimates for the displacement field and mean shear, one finds that, for the test conditions of figure 12, equation (12) is never satisfied, indicating that a position of zero density gradient does not exist in the flow. Hence, one would conclude that for this case the tendency toward wave overturning has been suppressed by viscosity, a result clearly in agreement with the observations.

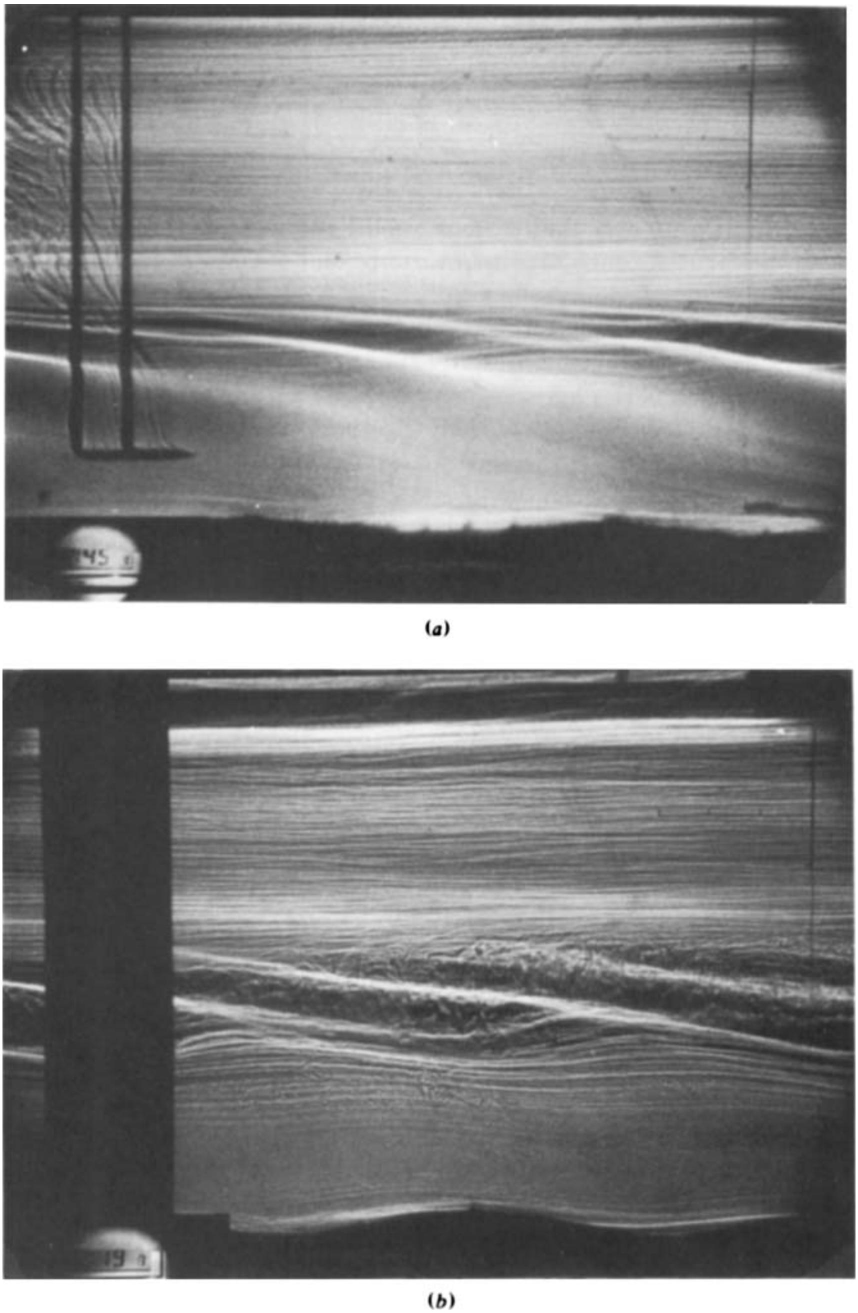

FIGURE 14. Wave field generated by 15 cm corrugated boundary. (*a*) Stable critical layer: $U_{\text{Tow}} \simeq 2\,\text{cm}\,\text{s}^{-1}$, $U_{\max} \simeq 3\,\text{cm}\,\text{s}^{-1}$. (*b*) Unstable critical layer: $U_{\text{Tow}} \simeq 4\,\text{cm}\,\text{s}^{-1}$, $U_{\max} \simeq 4{\cdot}5\,\text{cm}\,\text{s}^{-1}$.

To test the criterion more thoroughly, we attempted to produce experimentally a flow which was destabilized near the critical layer. Guided by equation (12) (and a suggestion of D. Fritts), a second corrugated boundary was constructed having a wavelength of 15 cm (additionally, ka was reduced to about 0·2 to alleviate the flow-separation problem). For a towing speed of 2 cm s^{-1} and a maximum fluid velocity of 3 cm s^{-1}, equation (12) predicts a stable critical layer. The experimental observation for this case, shown in figure 14 (*a*), corroborates this prediction. However, equation (12) predicts an unstable critical layer for a towing speed of 4 cm s^{-1} and a maximum fluid velocity of 4·5 cm s^{-1}. Figure 14 (*b*) shows the experimental results for this case, where a turbulent breakdown in the critical-layer region is clearly observed. We conclude, therefore, that the present stability criterion, based upon the viscous wave-action equation, leads to excellent qualitative agreement with our experimental results.

Finally, we remark that the exponential term in equation (12) becomes important when $\phi(z) = O(1)$. This occurs when $Z = O(Z'_\nu)$, where $Z'_\nu \equiv z_\nu Ri^{\frac{1}{2}}$, z_ν being the viscous length scale defined by Fritts & Geller (1976). Using as a criterion for stability the inequality $Z'_\nu > z_c$ (with z_c as defined by Fritts & Geller) one correctly predicts stability for figures 12 and 14 (*a*), and instability for figure 14 (*b*).

In the discussion thus far presented, attention has been focused on the effects of shear upon a monochromatic disturbance of large horizontal extent. It is also of interest to study how a shearing motion interacts with a disturbance that is broad-banded and spatially compact. The configuration we have in mind is the wave field generated by a two-dimensional cylinder moving in the direction of the mean current. For the case of a uniform current, this corresponds to the classic lee-wave problem which has been investigated by numerous authors, notably Long (1955), Lyra (1943) and Queney (1948). For the sheared problem, various layered models have been proposed (cf. Turner 1973), and at least one continuous-flow problem has been investigated numerically by Sawyer (1960). The important restriction common to all of these analyses is the exclusion of a critical layer. To the author's knowledge, the only analysis which considers critical-layer effects upon the wave field generated by a spatially compact source is that due to Mager (1974). Essentially, Mager considers the Booker–Bretherton problem with the infinite wavy wall replaced by a dipole source. The analysis proceeds formally by applying multidimensional stationary-phase techniques to evaluate asymptotically the space–time inversion integrals associated with the linearized internal wave equation. Two results of this analysis are deemed important for the present study. First, Mager notes that for finite time the critical layer (where the fluid velocity equals the horizontal speed of the dipole) acts to absorb the energy of the incoming waves and add momentum to the mean shearing motion. Secondly, it is found that within the neighbourhood of the critical layer the simultaneous neglect of nonlinear and viscous terms gives rise to a singularity in the horizontal component of velocity for infinite time. Hence, the two most important results of the Booker–Bretherton problem for a monochromatic disturbance also apply when the internal wave source is broad-banded and spatially compact.

To proceed experimentally, a circular cylinder of diameter 2·65 cm was mounted transversely across the tank and towed through the test section at various speeds. Figure 15 presents a sequence of photographs which depicts the wave field generated by the cylinder moving through a fluid medium which is in a quiescent state. One notices the presence of a turbulent wake behind the body, and a lee-wave pattern radiating energy into the upper regions of the tank (this is perhaps most clear in figure 15 (*c*)). In figure 15 (*a*) one also observes the region of upstream influence ahead of the cylinder which has been discussed by Browand & Winant (1972).

Figure 16 shows the same sequence of photographs when shear is present and a critical layer exists. The velocity profile for this case is superimposed on figure 16 (*a*)

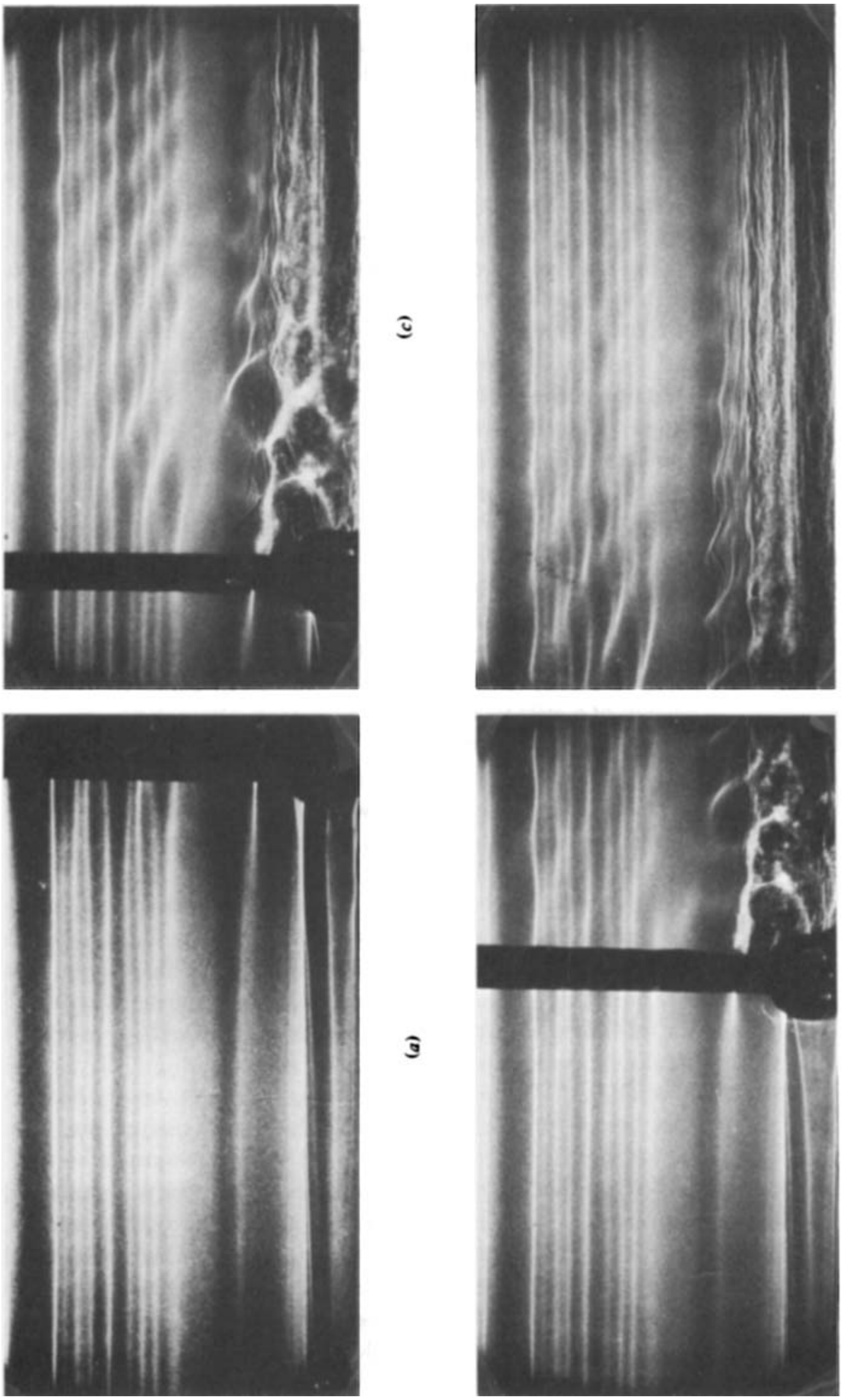

(a) (b) (c) (d)

FIGURE 15. Wave pattern generated by cylinder moving through quiescent fluid. Towing speed is 0·82 cm s^{-1}.

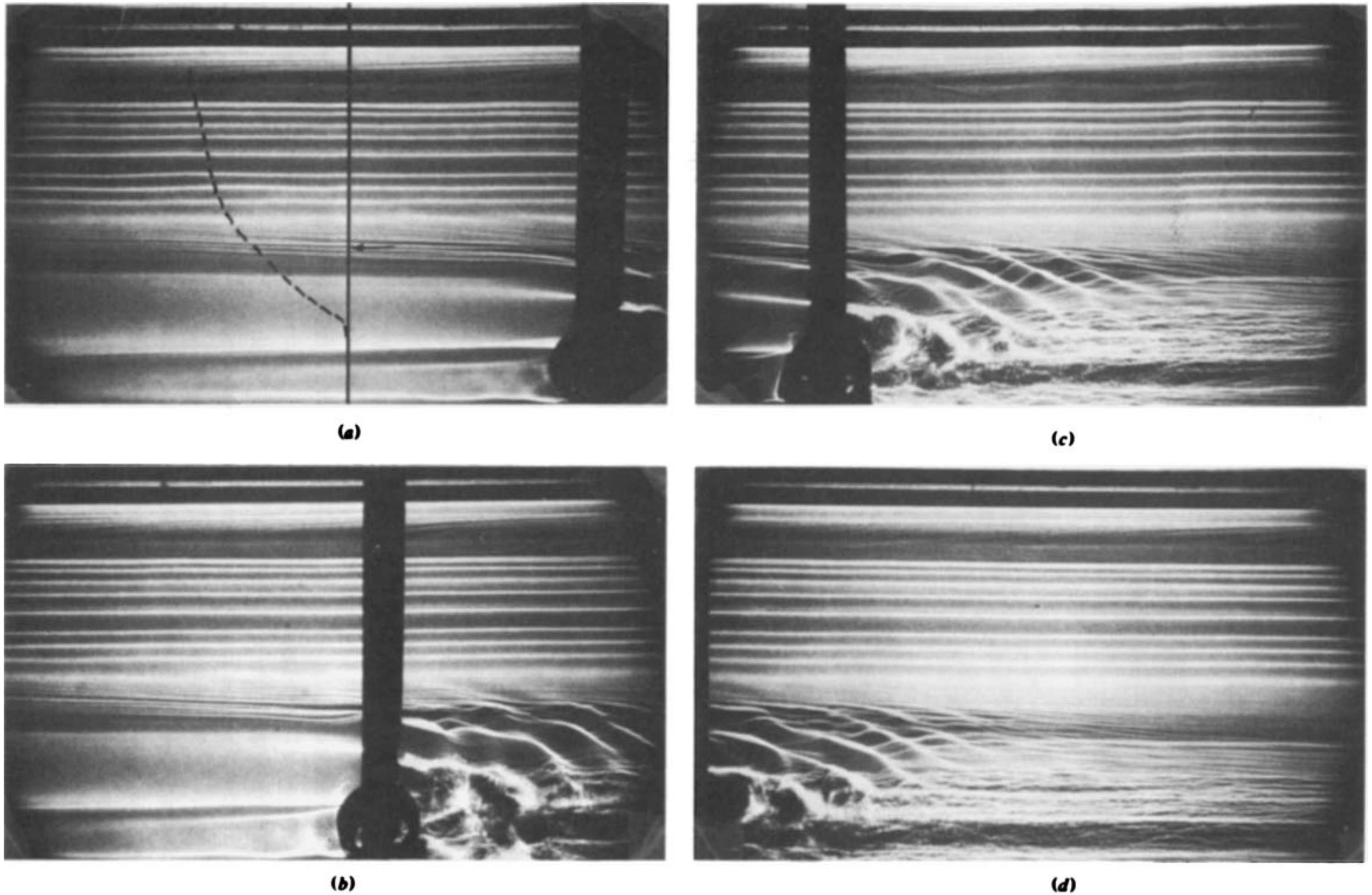

FIGURE 16. Wave pattern generated by cylinder moving through a shear flow when a critical layer exists. Measured velocity profile is shown superimposed on (*a*). Maximum fluid velocity is $1{\cdot}48\ \mathrm{cm\ s^{-1}}$ and the towing speed is $0{\cdot}82\ \mathrm{cm\ s^{-1}}$. The measured position of the critical layer is shown by an arrow.

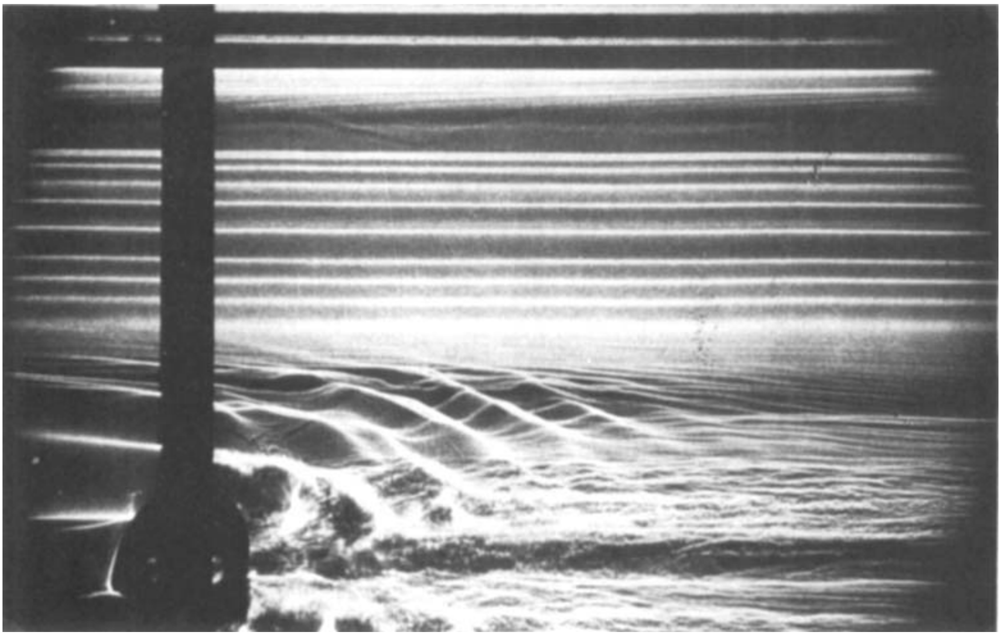

FIGURE 17. Enlargement of figure 16(*c*) showing detail of wave motion in the neighbourhood of the critical layer.

and the position of the critical layer is denoted by an arrow. The maximum fluid velocity in this case is $1{\cdot}48\ \mathrm{cm\ s^{-1}}$, and the towing speed is $0{\cdot}82\ \mathrm{cm\ s^{-1}}$. The global Richardson number for this case is $Ri \simeq 150$. One again sees that the effect of the critical layer is to transfer energy from the incoming waves to the mean shearing motion (or possibly reflect wave energy back towards the cylinder). Virtually no wave energy is observed above the critical layer. For visual clarity, figure 16 (*c*) has been enlarged and presented in figure 17 so that the details of the wave motion are more readily observable.

Comparing figures 15(*d*) and 16(*d*), one sees that a second effect of the shear is to increase the amplitude of the wave motions below the critical layer and to compress the region in space occupied by the wave field into a smaller volume. For example, in the unsheared case waves are visually observed to extend for almost 8 diameters downstream of the body. In the sheared case the wave field extended downstream for less than 4 diameters. Similarly, wave slopes in the unsheared case are typically $ka \simeq 0{\cdot}25$, as compared with $ka \simeq 0{\cdot}55$ in the sheared fluid.

In summarizing the results of the critical-layer experiments, we note that none of the internal-wave sources used generated a wave field sufficiently energetic as to penetrate the critical-layer region. However, a marked change in the character of the critical layer was observed as the importance of the nonlinearity relative to viscous effects was increased. This was evidenced by the critical-layer instability and turbulent breakdown observed in figure 14. At present, no more definitive statement may be made regarding the role of nonlinearity in critical-layer phenomenon, but more quantitative experimentation is proceeding presently. We also conclude from these experiments that the qualitative features of the waves near the critical layer are similar for the monochromatic wave field generated by the corrugated boundary and the broad-banded excitation of the circular cylinder.

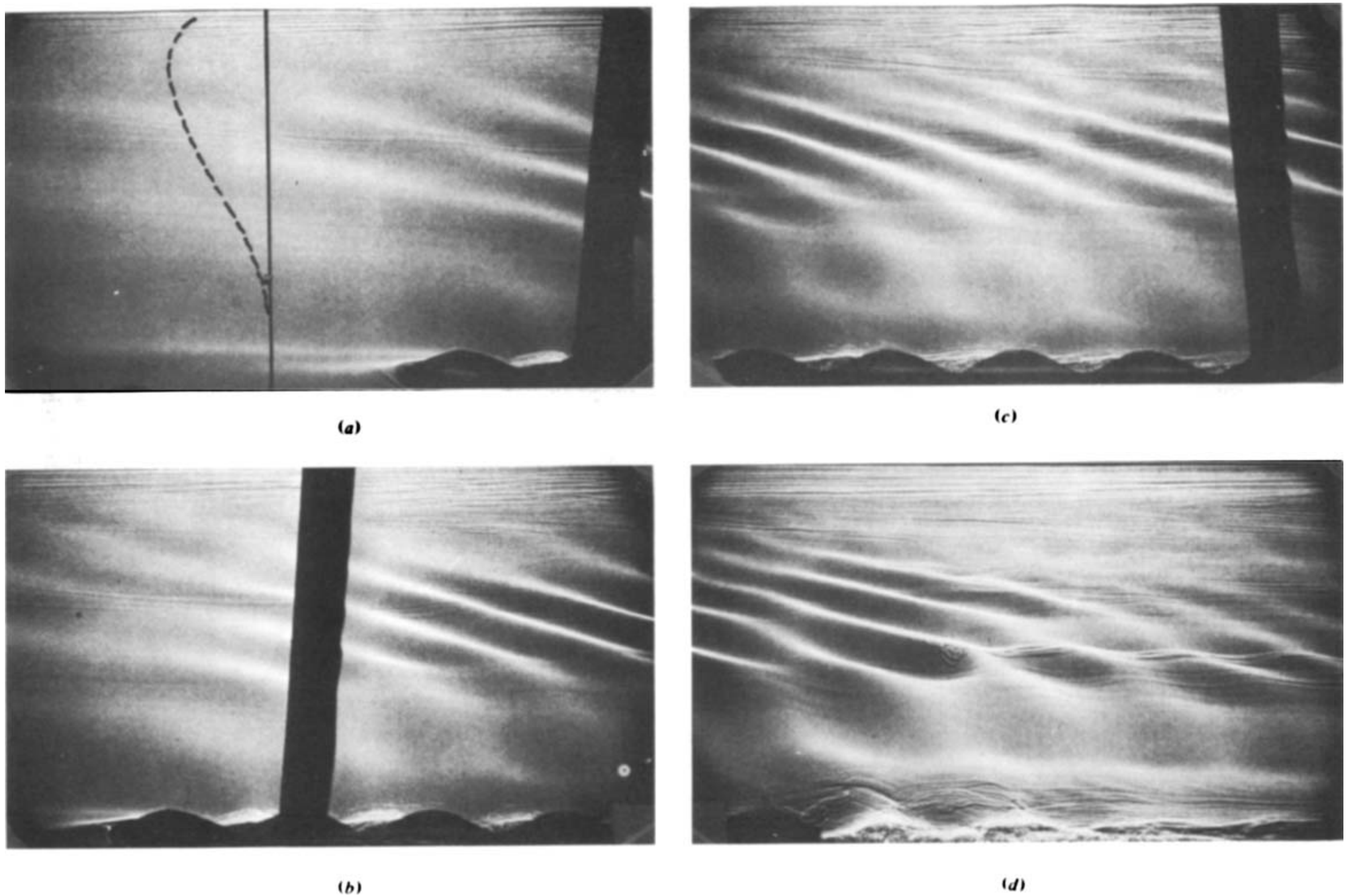

FIGURE 18. Wave pattern generated by wavy boundary moving through a shear flow when no critical layer exists. Measured velocity profile is superimposed on (*a*). The maximum fluid velocity is $1{\cdot}02$ cm s^{-1} and the towing speed is $2{\cdot}18$ cm s^{-1}.

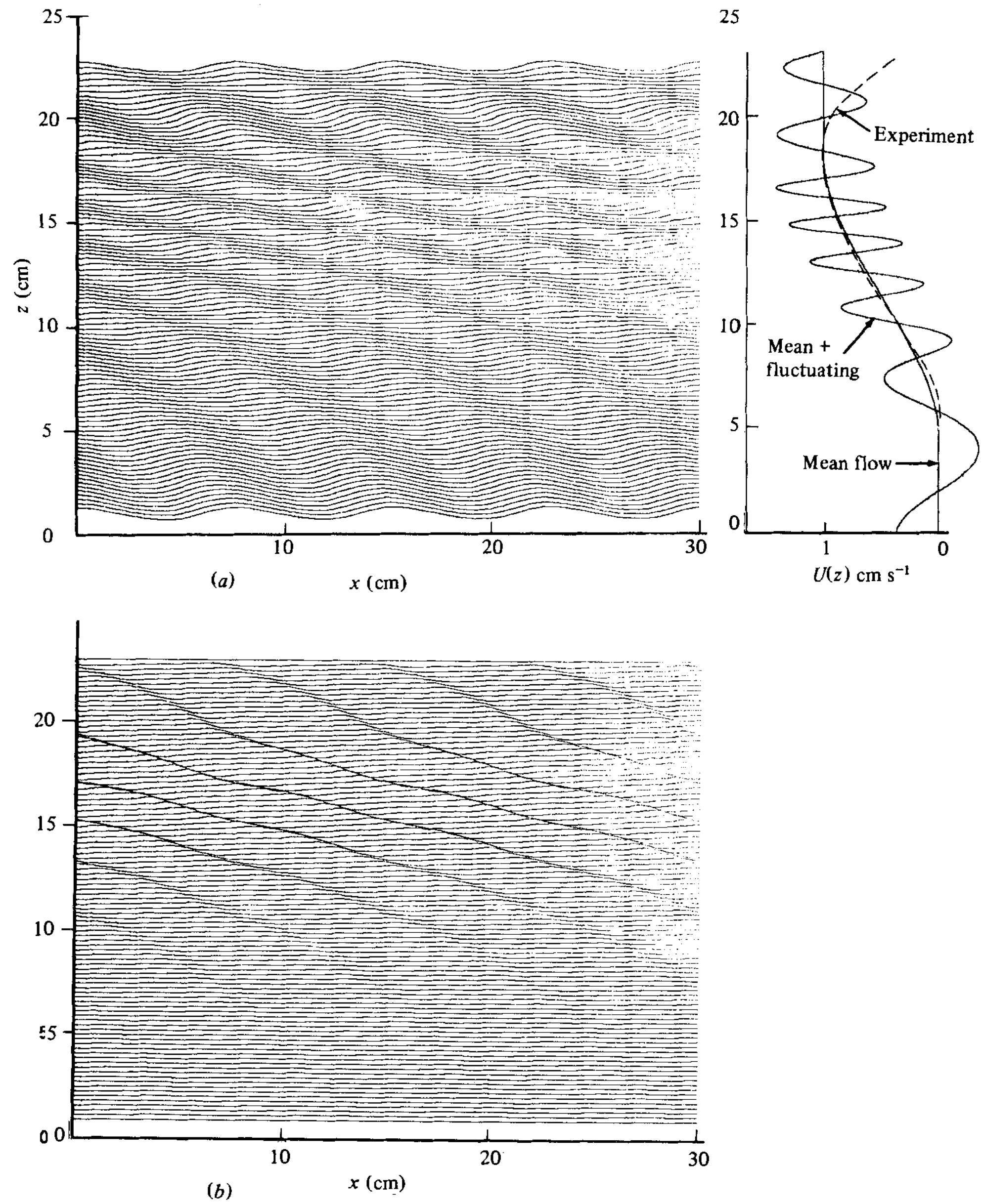

FIGURE 19. Wave field computed using wave-action theory for the experimental test conditions of figure 18. (a) Isopycnic displacement field. (b) Raster diagram of $\partial^2\rho/\partial z^2$.

5. Non-critical-layer flows

We now turn to a discussion of the results of some experiments conducted to study how internal waves interact with a shearing motion when a critical layer does not exist in the flow field. An important consideration in this part of the study was to see how well the observed wave patterns are describable by the aforementioned wave action model of equations (9)–(11).

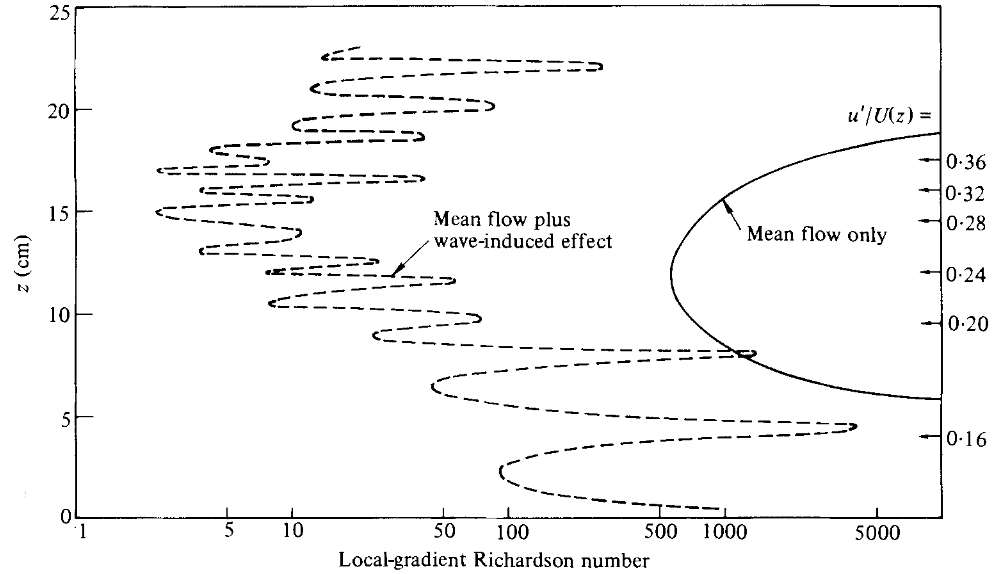

FIGURE 20. Computed distribution of the local-gradient Richardson number for the experimental test conditions of figure 18.

Figure 18 presents the results of an experiment performed using the 7·62 cm corrugated boundary. Here the towing speed of 2·18 cm s^{-1} exceeds the maximum fluid velocity of 1·02 cm s^{-1}, so that a critical level does not exist. For reference, the measured velocity profile is shown superimposed on figure 18(*a*). As anticipated for this non-critical-layer case, one observes that the shear does not act to trap the incoming waves, and the effects of the wavy boundary can be seen to extend throughout the tank. Constant phase lines within the shear region are seen to be inclined at an angle of about 17° with respect to the horizontal. We also see that within the sheared region the shadowgraph image is very intense. This is due to the Doppler-shifting effect of the shear upon the waves, giving rise to rapid phase changes in the vertical direction. Such phase changes result in large variations in the local density gradient, to which the shadowgraph is sensitive.

Equations (9)–(11) were used to compute the wave field generated by the corrugated boundary for this non-critical-layer case. The experimental test conditions were modelled assuming a constant-N density distribution (a good approximation over most of the depth) and a smooth velocity profile that closely matched the experimentally measured velocity over most of the depth. Figure 19(*a*) presents the computed isopycnic displacement field induced by the passage of the body. For reference, the velocity profile used in the calculations is shown along with the experimentally measured velocity distribution. As may be seen, there is good agreement between the profiles except near the top (above about $z = 21$ cm) where the experimental profile exhibits a boundary-layer-like distribution. One should not anticipate very good agreement between the theory and the experiments above this point. Also shown in figure 19(*a*) is the wave-induced horizontal velocity, which in some regions exceeds 30 % of the local mean velocity.

In examining these analytic results, one notes that the isopycnic displacements are largest near the body, but do not vary significantly through the medium. This is in contrast to our previous calculations near a critical layer where significant attenuation occurs. We also see that within the shear region a longitudinal asymmetry exists, with slopes on the downstream side of the waves being significantly steeper than those on the upstream side.

For comparison with the shadowgraph images of figure 18 (where image intensity is proportional to the second derivative of the density), the distribution of $\partial^2\rho'/\partial z^2$ (ρ' being the perturbed density field) was computed, and is presented in figure 19(*b*). In comparing this calculation with the data (particularly figure 18(*c*)) one sees a fair amount of qualitative agreement. Below the shear region, the second derivatives are quite small, suggesting that little contrast in the shadowgraph image should be observed here. Within the sheared region, large changes in the second derivatives are noted, suggesting sharp changes in contrast. Furthermore, the lines of constant phase in this region are oriented at an angle of about 15° with respect to the horizontal, quite consistent with experimental results. Above the sheared region, the comparison with the experimental results is not very good, but this is most likely due to variations in N which existed here coupled with the poor approximation to the measured velocity profile.

A further calculation which is also of some use is the effect of the wave-induced motions upon the local-gradient Richardson number. Figure 20 presents the vertical distribution of the quantity

$$Ri = -\frac{\dfrac{g}{\bar{\rho}}\left(\dfrac{\partial\bar{\rho}}{\partial z}+\dfrac{\partial\rho'}{\partial z}\right)}{\left(\dfrac{\partial\bar{U}}{\partial z}+\dfrac{\partial u'}{\partial z}\right)^2},$$

for the test conditions in figure 18. For comparison, the ambient Richardson-number distribution (i.e. in the absence of waves) is also presented. When there are no waves present, the Richardson number in the centre of the channel is about 570. The wave-induced contribution is seen to modify this distribution substantially, effecting more than a three-orders-of-magnitude reduction in the local Richardson number in some regions. Although the degree to which these calculations are quantitatively correct is somewhat questionable, the general conclusion may be made that the wave-induced part of the flow field is not small, and can significantly alter the distribution of the local-gradient Richardson number.

The results of these calculations, particularly the longitudinal asymmetry of the isopycnic displacements coupled with the dramatic alteration of the local-gradient Richardson number, are very suggestive of the possibility that even in the absence of a critical layer a sufficiently strong internal-wave/shear interaction may lead to the same convective overturning of waves noted in figure 14 and/or the growth of dynamical Kelvin–Helmholtz instabilities. We note from the work of Thorpe (1978), for example, that the slope of an internal wave at the point of incipient breaking may be significantly reduced by the presence of shear. Thorpe also observed a co-existence of turbulent motions induced by wave overturning and Kelvin–Helmholtz billows. Such wave-induced turbulent mixing would have a profound effect upon vertical diffusion processes in the ocean, although for realistic oceanic conditions the import-

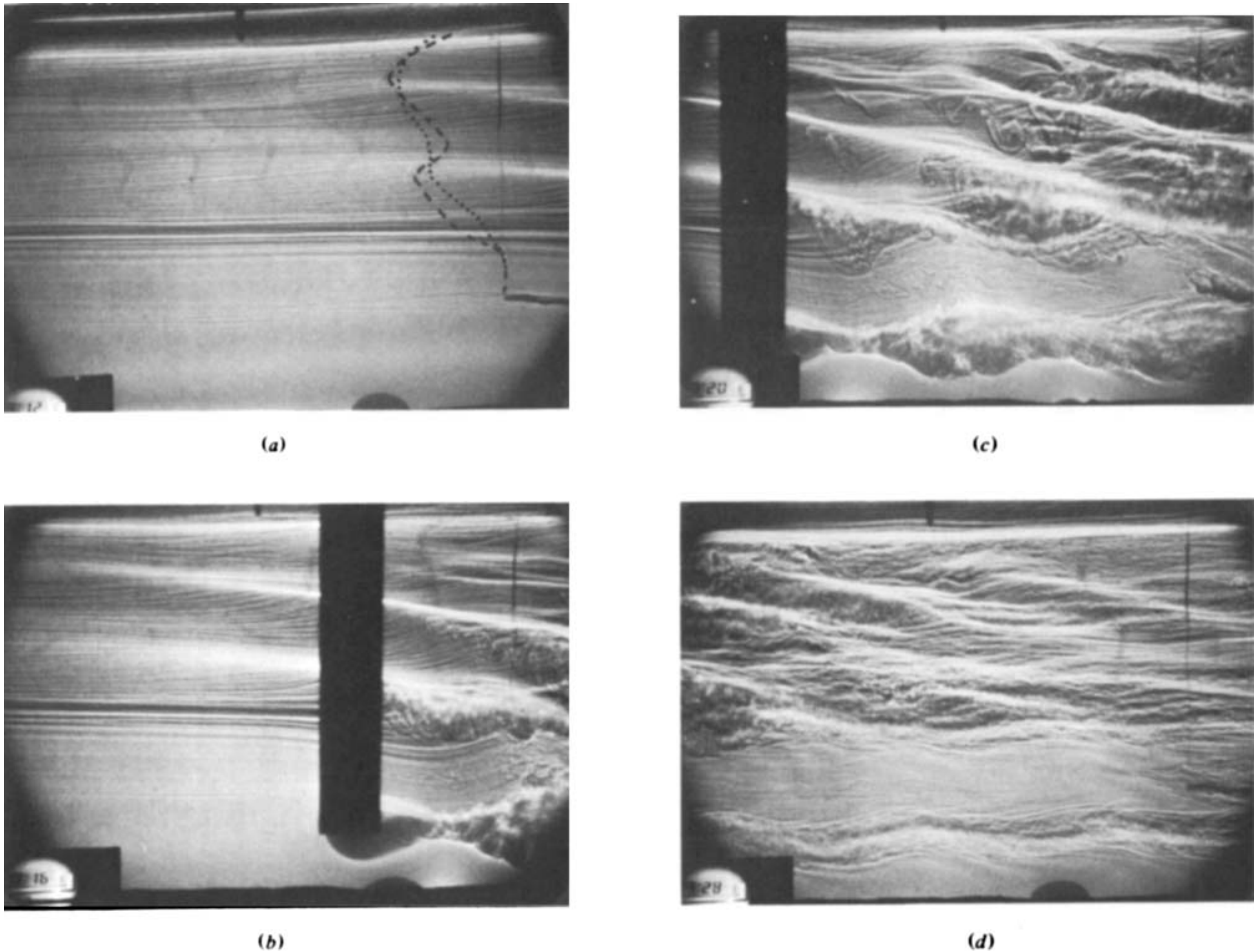

(*a*) (*c*)

(*b*) (*d*)

FIGURE 21. Wave pattern generated by cylinder moving through a shear flow when no critical layer exists. Note the severe distortion to the velocity profile in (*a*) (denoted by – – –) when waves are present, compared with the mean profile (denoted by · · · · ·). Towing speed $\simeq$ 4 cm s^{-1}, maximum fluid speed $\simeq$ 3 cm s^{-1}.

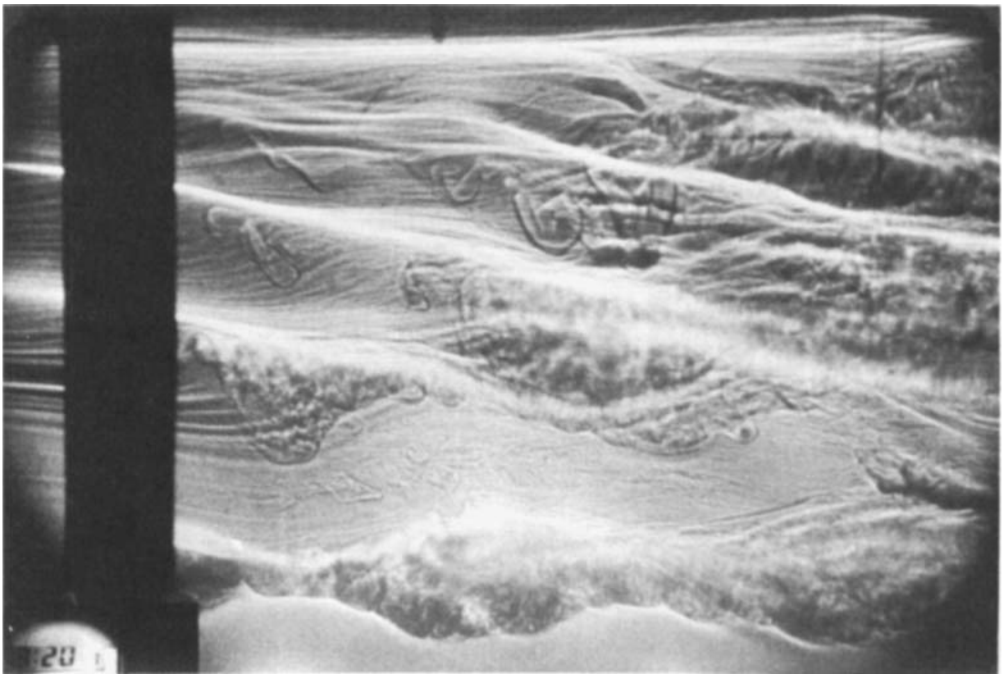

FIGURE 22. Enlargement of figure 21 (*c*) showing details of off-track turbulence generation.

ance of convective instability relative to Kelvin–Helmholtz induced turbulent mixing has not been fully assessed.

To pursue further the possibility of wave-induced turbulence in the absence of a critical layer, experiments were performed using the circular cylinder as the wave source (which tends to excite a fairly energetic wave field). Figure 21 presents the observed wave field generated by the cylinder when the towing speed exceeds the maximum fluid velocity so that no critical layer exists in the flow. The maximum fluid velocity for this case is about 2·9 cm s^{-1}, and the towing speed is 3·95 cm s^{-1}. The global Richardson number is $Ri \simeq 150$. The results of this experiment were somewhat surprising. As anticipated for this non-critical-layer case, the wave field is not trapped by the shear, and waves are seen to extend to the top of the tank. What is interesting, however, is the appearance of fine-scale turbulence downstream of the cylinder at vertical locations *several diameters above* the track of the cylinder motion. From an enlargement of figure 21 (*c*), shown in figure 22, one sees that the presence of these turbulent motions appears to be highly correlated with the lee-wave pattern generated by the cylinder. To show that the existence of this turbulence production is intimately related to the presence of shear, the above experiment was repeated with the fluid in a quiescent state. The results, depicted in figure 23, show none of the aforementioned off-track turbulence generation. One possible inference which could be drawn from these results is that somehow the lee-wave pattern radiating away from the body triggers an instability which subsequently grows to significant amplitude and degrades into turbulence. Such a wave-induced instability has been previously proposed as a mechanism for the generation of turbulent mixing in a marginally stable oceanic thermocline (cf. Woods 1968). What is somewhat surprising in the present experiment is that in the absence of any wave motion the minimum Richardson

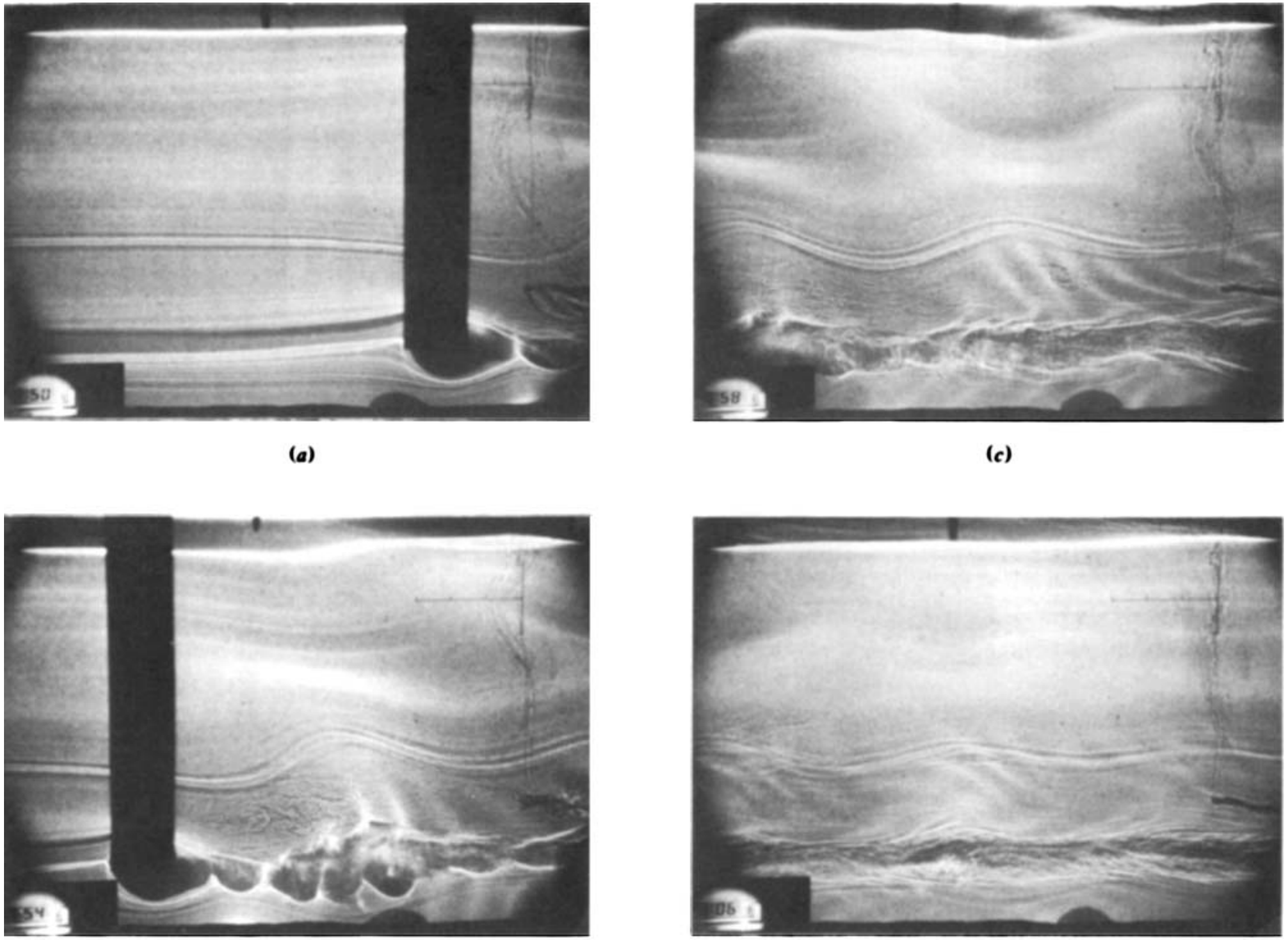

(a) (c)

(b) (d)

FIGURE 23. Wave pattern generated by cylinder moving through quiescent fluid. Towing speed $\simeq$ 4 cm s^{-1}.

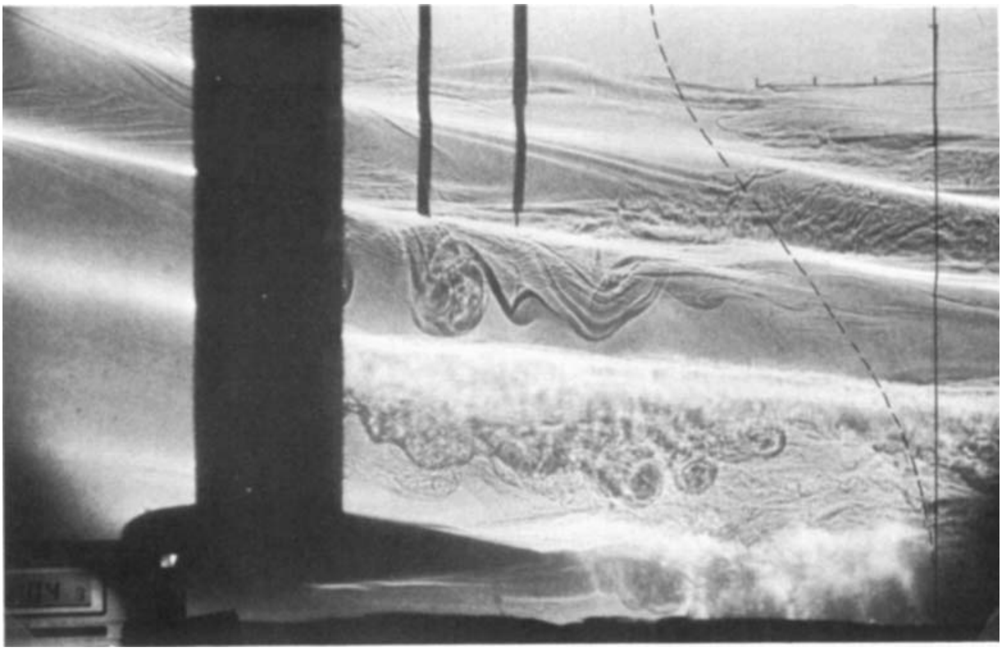

FIGURE 24. Wave pattern generated by an airfoil section moving through a shear flow when no critical layer exists. Measured velocity profile is shown superimposed on the figure, where the horizontal tick marks correspond to $0{\cdot}5\ \text{cm s}^{-1}$. Towing speed for this case is $3{\cdot}1\ \text{cm s}^{-1}$.

number is extremely large ($Ri \simeq 150$) when compared to the Richardson number normally required for dynamic instability, $Ri = 0{\cdot}25$, or convective instability $Ri < 0$. Clearly, if the instability is triggered by the wave motion, the wave-induced perturbations must (at least locally) dominate the flow in order that the stability boundary be transcended. Recalling, however, the previously presented Richardson-number calculations (figure 19), it is not unreasonable to expect that the wave-induced part of the flow field may be large enough to cause local instability.

To investigate the nature of this instability further, a brief experiment was performed to measure the wave-induced velocity and density perturbations in a region where local instability is observed. In order to reduce the effect of the large turbulent wake of the cylinder, an airfoil section (NACA 0018, chord length = 15 cm) was used. Quantitative measurements were made using a hot-film anemometer and a conductivity probe positioned 10·7 cm above the airfoil centre-line (the probe configuration and measured velocity profile for this experiment have been presented previously in figure 3). The sensors were fixed in laboratory co-ordinates, so that as the waves propagated behind the body, a measure of the horizontal structure of the flow field at a given vertical position was obtained. Figure 24 shows the shadowgraph image obtained at the point in time when a phase front just reached the probes. The airfoil is being towed at $3{\cdot}1\ \text{cm s}^{-1}$ and, from the velocity profile superimposed on this figure, the maximum fluid velocity was $2{\cdot}46\ \text{cm s}^{-1}$. As was observed for the cylinder experiments, turbulence highly correlated with the wave field exists above the airfoil. The ambient global Richardson number for this case was $Ri = 183$. Figure 25 presents time traces of the velocity and density fields measured for this case. An arrow denotes

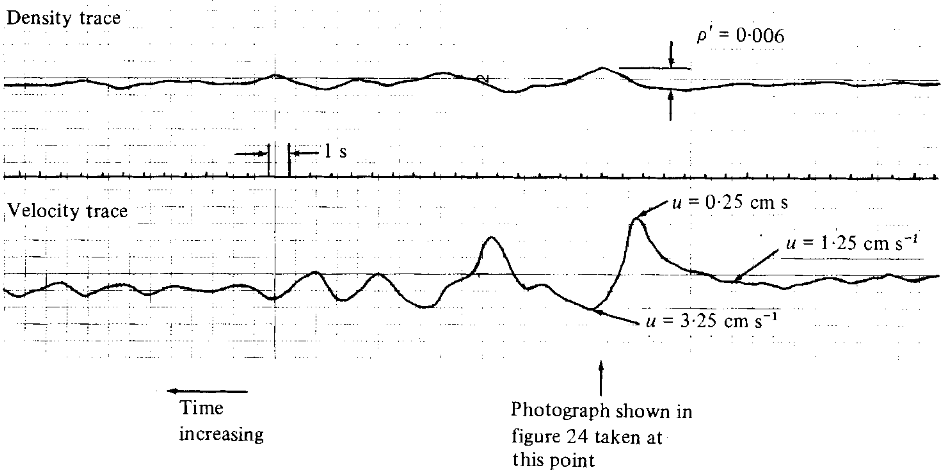

FIGURE 25. Velocity and density measurements obtained in the wave field generated by the moving airfoil shown in figure 24.

the point in time when the photograph of figure 24 was taken. The maximum wave-induced density perturbation is measured to be about $\rho' = 0{\cdot}006\ \mathrm{g\ cm^{-3}}$, corresponding to a peak–peak displacement of 1·02 cm. From the velocity trace one finds that a maximum velocity of $3{\cdot}25\ \mathrm{cm\ s^{-1}}$ is observed. The ambient fluid velocity at this point is $1{\cdot}25\ \mathrm{cm\ s^{-1}}$, and the towing speed (and hence the wave phase speed) is $3{\cdot}1\ \mathrm{cm\ s^{-1}}$. At this location, then, the local fluid velocity slightly exceeds the phase speed by $0{\cdot}15\ \mathrm{cm\ s^{-1}}$. This is exactly the criterion required for the existence of the wave-overturning phenomenon discussed by Orlanski & Bryan (1969). Additionally, we note from scaling the photograph that the product of the vertical wavenumber times the wave amplitude is roughly $k_z a \simeq 0{\cdot}9$ (a being equal to half the peak–peak amplitude) which is also very close to the criterion for convective overturning proposed by Orlanski (1972). We conclude, therefore, that the turbulent motions observed at the phase front in this figure are most likely the result of an instability which is convective in nature.

One may also use these data to estimate the wave effect on the local-gradient Richardson number. However, the measurements (which describe the horizontal distribution of the flow field) are not directly applicable, as one really needs information about the vertical gradients. If one is willing to assume,† though, that

$$\frac{\partial}{\partial z} = \frac{1}{\tan\theta}\frac{\partial}{\partial x},$$

where θ is the angle of the constant-phase line with respect to the horizontal, one may use the measured data to estimate the local gradient Richardson number. Determining θ from the shadowgraph image, the minimum-gradient Richardson number is measured to be $Ri = 0{\cdot}60$. Considering that the ambient value of the Richardson number is $Ri = 180$, we see that the wave-induced motion has a profound effect upon the local stability of the system.

† In a flow field where overturning waves are present, however, such an approximation may not be valid.

6. Summary

The results of an experimental investigation dealing with the interaction of internal waves with a mean shearing motion have been presented. The first experiments extended the work of Mowbray & Rarity (1967) to examine the effects of density and velocity structure upon the wave field generated by an oscillating cylinder. The results, which were interpreted in terms of a WKB approximation to the linearized internal wave equation, showed that waves may be reflected or absorbed by the presence of shear, depending upon the direction of propagation relative to that of the fluid.

A second series of experiments dealt with the wave pattern generated by a wavy boundary in the presence of a critical layer, a problem considered theoretically by Booker & Bretherton (1967). Of particular concern was the determination of whether the effects on nonlinearity anticipated from the recent work of Stewartson (1978), Brown & Stewartson (1980), Warn & Warn (1978) and Fritts (1978, 1979) could be observed experimentally. It was concluded for the present experiment that, if nonlinearity manifested in the form of harmonic generation, critical-layer transmission or reflection was important, its effects were masked by the simultaneous importance of viscosity. One nonlinear effect which was observed, however, was the turbulence induced by a convective instability near the critical layer. A stability criterion, based upon the viscous wave-action equation, correctly predicted the boundary between stable- and unstable-critical-level flows. Experiments were also conducted using the wavy boundary to investigate the wave field in a non-critical-layer case. The results were compared with calculations based upon the conservation of wave-action flux, and good qualitative agreement was observed. These calculations also indicated that the wave-induced perturbations can substantially alter the local-gradient Richardson-number distribution.

Finally, experimental results on the wave field generated by a compact source were presented. The cylinder results show that, as in the wavy-wall experiments, the effect of shear on a broad-banded spatially compact source is to trap wave energy below the critical layer. For the non-critical-layer case, where the towing speed exceeded the maximum fluid velocity, an interesting result was obtained. Turbulent motions highly correlated with the wave field were observed at vertical positions several body diameters removed from the track of the cylinder motion. Subsequent velocity and density measurements, made behind an airfoil section where similar phenomena were observed, revealed that the wave-induced perturbations can effect reductions in the local Richardson number to such an extent that dynamic instabilities may develop. These measurements are also suggestive of the possibility that wave overturning may be responsible for the observed turbulence production. Such wave-induced turbulence is almost certain to be significant with regard to mixing processes in both the ocean and the atmosphere, and further experimentation designed to address quantitatively some of the important aspects of this problem is presently under way.

This work was sponsored by the Applied Physics Laboratory of The Johns Hopkins University under Contract Number APL/JHU 601038. The assistance of Drs B. M. Lake and C. L. Hindman and Prof. L. G. Redekopp, who participated in several useful discussions during the course of this work, is gratefully acknowledged. Prof. E. Y. Hsu and Mr D. Rowland are also acknowledged for their efforts in the designing and building of the experimental apparatus, and Mr B. McGee for his assistance in running the experiments.

REFERENCES

Beland, M. 1978 The evolution of a nonlinear Rossby-wave critical layer: effect of viscosity. *J. Atmos. Sci.* **35**, 1802.

Booker, J. & Bretherton, F. 1967 The critical layer for internal gravity waves in a shear flow. *J. Fluid Mech.* **27**, 513.

Bretherton, F. 1966 The propagation of groups of internal gravity waves in a shear flow. *Quart. J. Roy. Met. Soc.* A **92**, 466.

Browand, F. & Winant, C. 1972 Blocking ahead of a cylinder moving in a stratified fluid: an experiment. *Geophys. Fluid Dyn.* **4**, 29.

Brown, S. & Stewartson, K. 1980 On the nonlinear reflection of a gravity wave at a critical layer. *J. Fluid Mech.* **100**, 577.

Dickinson, R. 1970 Development of a Rossby-wave critical level. *J. Atmos. Sci.* **27**, 627.

Fritts, D. 1978 The nonlinear gravity-wave/critical-level interaction. *J. Atmos. Sci.* **35**, 397.

Fritts, D. 1979 The excitation of radiating waves and Kelvin–Helmholtz instabilities by the gravity-wave critical-level interaction. *J. Atmos. Sci.* **26**, 12.

Fritts, D. & Geller, M. 1976 Viscous stabilization of gravity-wave critical-level flows. *J. Atmos. Sci.* **33**, 2276.

Geller, M., Tanaka, H. & Fritts, D. 1975 Production of turbulence in the vicinity of critical layers for internal gravity waves. *J. Atmos. Sci.* **32**, 2125.

Grimshaw, R. 1974 Internal gravity waves in a slow varying dissipative medium. *Geophys. Fluid Dyn.* **6**, 131.

Haberman, R. 1972 Critical layers in a parallel flow. *Stud. Appl. Math.* **51**, 139.

Hazel, P. 1967 The effect of viscosity and heat conduction on internal gravity waves at a critical level. *J. Fluid Mech.* **30**, 775.

Jones, W. & Houghton, D. 1971 The coupling of momentum between internal gravity waves and mean flow: a numerical study. *J. Atmos. Sci.* **28**, 604.

Long, R. 1955 Some aspects of the flow of stratified fluid. III. Continuous density gradients. *Tellus* **7**, 342.

Lyra, G. 1943 Theorie der stationären Leewellenströmung in freier Atmosphäre. *Z. angew. Math. Mech.* **23**, 1.

Mager, R. 1974 Internal gravity waves generated by a moving source in a stratified fluid. *Denver Research Institute Rep. No.* DRI MS-R-7502, Univ. of Denver, Denver, Colorado.

Maslowe, S. 1972 The generation of clear-air turbulence by nonlinear waves. *Stud. Appl. Math.* **51**, 1.

Mowbray, D. & Rarity, B. 1967 A theoretical and experimental investigation of the phase configuration of internal waves of small amplitude in a density-stratified liquid. *J. Fluid Mech.* **28**, 1.

Odell, G. & Kovasznay, L. 1971 A new type of water channel with density stratification. *J. Fluid Mech.* **50**, 535.

Orlanski, I. & Bryan, K. 1969 Formation of the thermocline step structure by large-amplitude internal gravity waves. *J. Geophys. Res.* **74**, 6975.

Orlanski, I. 1972 On the breaking of standing internal gravity waves. *J. Fluid Mech.* **54**, 577.

Phillips, O. 1966 *Dynamics of the Upper Ocean.* Cambridge University Press.

Queney, P. 1948 The problem of air flow over mountains: a summary of theoretical studies *Bull. Am. Met. Soc.* **29**, 16.

Sanford, T. 1975 Observation of the vertical structure of internal waves. *J. Geophys. Res.* **80**, 3861.

Sawyer, J. 1960 A numerical calculation of the displacements of a stratified airstream crossing. a ridge of small height. *Quart. J. Roy. Met. Soc.* **86**, 326.

STEWARTSON, K. 1978 The evolution of the critical level of a Rossby wave. *Geophys. Astrophys. Fluid Dyn.* **9**, 185.

THORPE, S. 1978 On the shape and breaking of internal gravity waves in a shear flow. *J. Fluid Mech.* **85**, 7.

TURNER, J. 1973 *Buoyancy Effects in Fluids*. Cambridge University Press.

WARN, T. & WARN, H. 1978 The evolution of a nonlinear critical layer. *Stud. Appl. Math.* **59**, 37.

WOODS, J. 1968 Wave induced shear instability in the Summer thermocline. *J. Fluid Mech.* **32**, 791.